Microfluidic Large Scale Integration and its Application in Image Based Microflow Cytometry

by

Bo Yang Yu

A thesis
presented to the University of Waterloo
in fulfillment of the
thesis requirement for the degree of
Master of Applied Science
in
Mechanical Engineering

Waterloo, Ontario, Canada, 2010

Author's Declaration

I hereby declare that I am the sole author of this thesis. This is a true copy of the thesis, including any required final revisions, as accepted by my examiners.

I understand that my thesis may be made electronically available to the public.

Bo Yang Yu

Abstract

Microfluidic Large Scale Integration (mLSI) is a technology that can integrate thousands of microvalves, pumps and compartments in a single chip. The most significant advantage of mLSI is its high degree of integration which enables complex fluid manipulation and fully automated chemical/biological assays. mLSI allows the integration of multiple devices onto one chip thus significantly reducing the space requirement, and the fully automated valve system considerably improved the throughput.

The first sub-project in this thesis work focused on the development of an mLSI platform in the Waterloo Microfluidic Laboratory (WML) for the fabrication and control of Microfluidic devices with integrated control valves. Fabrication guidelines are available from previously published literature and are tested and modified according to the facilities available in WML. A large scale valve control system is assembled, capable of controlling 32 individual microvalves and 8 micropumps. The physical properties of the microvalves and pumps, including optimal dimensions, actuation frequency, and pumping rates, are studied using analytical models as well as experimental measurements. The micro fabrication guidelines, design and operating principles of the control system, and optimal design parameters for the microvalves are all documented in this thesis as well as design recommendations for future improvements.

The second sub-project of this thesis work is focused on designing an intelligent flow cytometry system with microscopic imaging detection. The goal of this system is to automate the yeast cell cycle classification procedure used in biological studies. Microscopic imaging detection is chosen over conventional optical sensors for its ability to extract morphological properties from cells, which is the main criterion in yeast cell cycle identification. And mLSI technologies are used for fluid control for reduced sized and the ease of automation.

An intelligent image processing algorithm is first designed to automatically classify microscopic images of yeast cells in a microfluidic channel environment. The development

process used stationary cell images as training data. The images are enhanced to reduce background noise, and a robust segmentation algorithm is developed to extract geometrical features including compactness, axis ratio, and bud size. The features are then used for classification, and the accuracies of various machine-learning classification algorithms are compared. The linear support vector machine, distance-based classification, and k-nearest-neighbour algorithm were the classifiers used. The performance variations of the system under various illumination and focusing conditions are also tested. The results suggest it is possible to automatically classify yeast cells based on their morphological characteristics with noisy and low-contrast images.

A micro fabricated cell sorter chip is then designed for the purpose of cell sorting using the above mentioned algorithm. A review of existing cytometry techniques is conducted to justify the choices of detection and flow control technologies. Then the chip structure is designed. Experiments are conducted with different channel dimensions and chip layouts to optimize the fabrication process and sample focusing performances, a sorting simulation is conducted using fluorescent beads to optimize the detection system parameters and verify the sorting accuracy. A cell counting experiment is also performed, the system was able to detect and classify cells with very high accuracy, with a throughput of 1.5 cells per second. Due to equipment and time limitation, cell sorting was not verified.

This thesis project shows the goal of implementing mLSI at WML was successfully achieved, and imaging detection and mLSI can be used to produce a cell sorter capable of detecting and classifying yeast cells in different cell cycle phases. Recommendations are made at the end for improvements in the mLSI system, and the application of the cell sorter in detecting protein factors in budding yeast cells.

Acknowledgements

I would like to thank my two supervisors, Dr Carolyn Ren and Dr Jan Huissoon, for their continued support over the last four years through both my Bachelor and Master degrees. Their suggestions and encouragements have always guided me to break through the various challenges I faced. Their knowledge and experiences have influenced my growth over these years in many ways.

I would also like to thank every member of the Waterloo Microfluidic Laboratory: the senior members, especially Caglar Elbuken, Tom Glawdel, Mostafa Shameli, Zeyad Almutairi and Lin Gui, for their friendliness and professionalism, and showing me tirelessly the skills necessary to become a good researcher; also the co-op students, Chong Shen, Danny Chan, and Andrew Carnovale for their youth and energy, and helping me perfecting every single detail of this thesis project.

I am extremely grateful and proud to be a graduate of the combined Bachelor/Master degree in Mechanical and Mechatronics Engineering at the University of Waterloo. The Mechatronics Engineering undergraduate program was excellent in teaching me a variety of technical and theoretical skills, and the one year master programs allow me to receive exceptional education in a short time span. The financial support provided by MME department and Natural Sciences and Engineering Research Council of Canada (NSERC) is also greatly appreciated.

Special thanks to all my friends and family for all the fun and laughter, also the support during the tough times. Thank you to my parents RongSheng Yu and ShuHui Liu, for believing in me throughout the years; to Ali Hussaini, Hasan Toplar, Rao Ge and Wu Ge for sticking with me all along the way. And to my lovingly mistress Yili, if not for her continued motivation and support, I would not be here today.

Table of Contents

List of Figures

List of Tables

Nomenclature

Acronyms:

CCD	charged coupled device
DI	de-ionized
Fps	frame per second
GED	generalized Euclidean distance
HDMS	hexamethyldisilazne
I/O (DIO)	input/output (digital input/output)
KCL	Kirchhoff's current law
kNN	kth nearest neighbour
LCD	liquid crystal display
LED	light emitting diode
mLSI	microfluidic Large Scale Integration
OS	operating system
PC	personal computer
PCB	printed circuit board
PDMS	polydimethylsiloxane
PEG	polyethylene glycol
PMT	photo-multiplier tube
ROI	region of interest
SVM	support vector machine

Mathematical Symbols:

A	area
A_X	user-defined amplification factor
C	fluidic capacitance
c	compactness
$Conc$	concentration
E	Young's Modulus
f_c	cut-off frequency
f_{pump}	pumping frequency
h	channel height
L	membrane length
n	user-defined threshold value
p	perimeter
$p_{i,j}$	pixel intensity at index (i,j)
P	pressure
q	flow rate
R	fluidic channel resistance
T	membrane thickness
V	volume
w	channel width
μ	mean
σ	standard deviation
δ_{max}	maximum membrane deflection

Chapter 1. Introduction

1.1 Objective and Outline

The introduction of microfluidic large scale integration (mLSI) a decade ago provided a simple and effective technology platform for the development of highly integrated microfluidic lab-on-a-chip devices. Microfluidic large scale integration refers to the development of microfluidic chips with thousands of integrated micro valves. [Melin 2007] This technology enabled hundreds of assays to be performed in parallel with multiple reagents in an automated manner. Since its introduction, it had been applied to a variety of biological and chemical analyses. [Melin 2007]

A successful application of mLSI had been in flow cytometry. [Fu 2002] Flow cytometry refers to the counting and measurement of cells and their various parameters in a flowing liquid media. A flow cytometer with integrated valves was capable of conducting single cell studies due to its high precision flow control [Fu 2002]. Meanwhile, the advancements in camera technologies and microscopy made microscopic image analysis a viable detection method for flow cytometer, this resulted in the possibility of performing cell morphological analyses in flow cytometry.

Cell morphology identification is a vital step in the study of cell cycle modelling, since the most common model species for cell cycle studies, Saccharomyces cerevisiae (common yeast cell), shows distinctive morphological variations in different stages of its division cycle. Yeast cells could be classified into different cell cycle phases by a human observer, and this method was subjective and inefficient. Thus, an image based flow cytometer with integrate valves could find its application in the morphological studies of yeast cells.

The goal of my work in the past two years was to gain greater understandings of mLSI by introducing this technology to the Waterloo Microfluidic Laboratory, and to apply the technology of mLSI in the development an image based flow cytometer with integrated microvalves, with the capability of identifying and sorting yeast cells in different cell cycle phases. Chapter 2 of this thesis listed all the chemicals and equipments used for this thesis work. The operating and design principles, along with the detailed fabrication procedures and

control strategies of mLSI were documented in chapter 3 of this thesis; while the design and operation of the flow cytometer was presented in chapters 4 and 5, in which the image analysis algorithm (chapter 4) and the chip design criteria (chapter 5) were both explained in details; finally in chapter 6 I recommended future applications of the flow cytometer to the study of cell cycle modelling.

In the remaining portions of this chapter I will briefly describe the principles of microfluidic large scale integration (section 1.2), the importance of cell cycle modelling (1.3) and the existing techniques in flow cytometry (1.4) to give the reader complete background information related to this thesis.

1.2 Microfluidic Large Scale Integration

Microfluidics is the control of fluid flow in sub-micro dimensional scale. It is commonly used in lab-on-a-chip applications for chemical and biological analyses. [Dittrich 2006; Melin 2007] However, traditional fluid control components such as mechanical valves and pumps are very difficult to miniaturize, while electrokinetic fluid manipulation methods are very sensitive to fluid properties such as PH value and surface properties. These fluid control methods are also difficult to fabricate in great number, thus limiting the early microfluidic devices to contain only a handful of valves and pumps. [Thorsen 2002]

In 2000, a research group led by Dr. Stephen Quake introduced their newest creation: monolithic microfabricated valves, to the microfluidic academic world. The microvalves used crossed-channel architecture, shown in Figure 1 below. The membrane separating the top and bottom channels was relatively thin (10 ~ 30 um). When pressure was applied to the lower channel ("control channel"), the membrane deflected upward and alters the fluid flow in the upper channel ("flow channel").

This new type of microvalve could be fabricated easily using soft lithography, a technique commonly used in microfluidic research labs for rapid prototyping of elastomeric microchips, and controlled electronically through the use of pressurized air. [Unger 2000] Combinations of the microvalves resulted in many distinctive functional components such as pumps, mixers,

and multiplexers, [Thorsen 2002] many of which had revolutionized the existing fluid control technologies. Most importantly the new microvalve can be fabricated in large numbers with very small foot print, literally allowing thousands of valves and pumps to be made on a single chip the size of a microscope slide, and thus the name: microfluidic large scale integration (mLSI). The microvalve itself gained much popularity in the years to come, and is commonly referred to by its founder: the Quake valve. [Landers 2008]

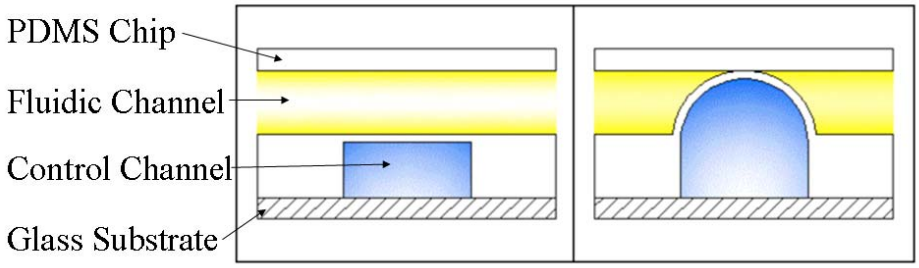

Figure 1 Illustration of Microvalve Working Principle

However, the Quake valve also has some disadvantages. The flow channel must have a rounded cross section in order for the valve to completely seal, and the channel dimensions were limited to low aspect ratio channels only. The pump has limited bandwidth: its performance would suffer if switched faster than 100Hz. Also, a peristaltic pump created with Quake valves suffers from pulsing effects and cannot produce constant fluid flow.

This research project was aimed at adapting the mLSI technology in the Waterloo Microfluidic Laboratory. The necessary steps included testing and adapting fabrication methods in our laboratory equipment, design and manufacture the control system, and investigate methods for improvement.

1.3 Cell Cycle modeling

A complete life cycle of eukaryotic cells would normally be divided into four phases: first gap phase (G_1 phase), synthesis phase (S phase), mitosis phase (M phase) and second gap phase (G_2 phase). The process of DNA replication, which is regulated by several control mechanisms, would happen in the S phase. Following the S phase, replicated chromosomes separate during the M phase and segregate in two nuclei that eventually will be endowed to each newborn daughter cell at cell division. The G_1 phase and G_2 phase separate cell birth from the S phase,

and the S phase from the M phase, respectively.

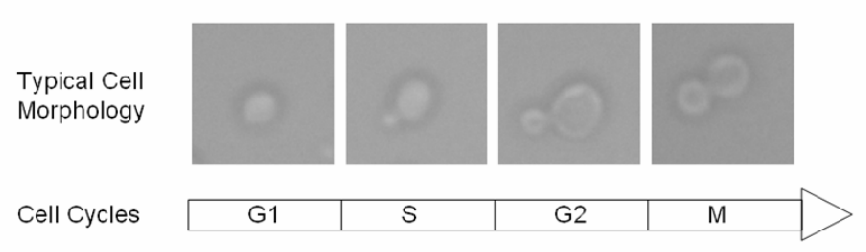

Figure 2 Yeast cell morphology through cell cycle progression

Understanding cell cycle regulation is of vital importance to the understanding of cancer development [Ingalls 2007]. The budding yeast cells, Saccharomyces cerevisiae, were frequently used as a model species in the study of cell cycles, because the basic elements of the yeast cell's structure are extensively homologous to those in higher plant and animal cells [Chen 2004], and that yeast cell cycle progression could be easily monitored via changes in cell morphology [Hartwell 1974; Herskowitz 1988]. As shown in Figure 2, cells in the G_1 phase are characterized by a simple ellipsoidal shape. When cells enter the S phase a bud emerges and is readily visible, and as the bud size grows larger, the cell enters the M phase. The ability to accurately identify yeast cells in different division phases, especially cells in the S phase, is critical in the modelling of cell cycles [Sidorova 2003; Ingalls 2007]. Conventional classification of the cell cycle was done manually, which was often subjective and time-consuming [Ohnuki 2009]. There was also no effective method for collecting and isolating cells in the phase of interest. The development of an automated device that could identify and isolate cells in a particular cell cycle phase was thus crucial to the systematic study of cell cycle modelling. In this thesis an automated microfluidic device that was capable of identifying and isolating S-phase yeast cells was described.

Several image-based yeast cell morphology identification devices/algorithms had been described previously. However, the existing methods were often equipment/fluorescent dependent, and were not easily adaptable under noisy conditions. A portion of this thesis is thus focused on developing an image-based pattern recognition algorithm that is capable of identifying yeast cell cycle phases, with the aim of applying this algorithm to microfluidic flow cytometry.

1.4 Flow Cytometry

Cytometry refers to the measurement of various parameters of cells, while flow cytometry is the cytometric analysis of cells in a flowing liquid media. Flow cytometry often includes the sorting of cells via controlling the flow network, and thus flow cytometers are also referred to as cell sorters. Commercial flow cytometry technologies are well developed with numerous available products and the capabilities of providing rapid and reliable analyses. The analytical capabilities of flow cytometry are finding increasing applications in cancer diagnosis [Rieseberg 2001], pharmacology [Andersson 2003], genetic research [Huh 2005], and food and water quality monitoring [Yamaguchi 2003].

However, commercial flow cytometry systems are also typically bulky, expensive, mechanically complex, and required specialized operators and high volume of the sample [Huh 2005]. These drawbacks had motivated efforts to design micro fabricated microfluidic devices to achieve smaller, simpler, and inexpensive microflow cytometers. Many of the exiting microflow cytometers would detect and measure cells by optically sensing the fluorescence and light scattering of cells passing through its detection units, and would deflect cells into different flow paths using dielectrophoresis force or electrokinetic flow switching. Optical sensors are popular due to the ability to integrate miniaturized optical devices, such as waveguides and lenses, on a microfluidic chip, yet the fabrication of multiple integrated optical sensors is a challenging process. Electrical manipulation of cells is also easy to miniaturize, but is potentially unsafe to bioparticles and requires complex fabrication of on-chip electrodes.

Image based detection (Figure 3), compared to optical sensors, is limited in speed and is difficult to miniaturize, but is more accurate and less prone to environment noise. Image based detection can also easily measure a variety of cell parameters whereas optical sensors need an increased the number of detectors to capture more information. For this research project – designing an automated device for yeast cell cycle identification – image based detection was chosen over optical detection for its low cost, availability of equipment (laboratory microscope and computer), and ability to investigate cell morphological properties. The integrated monolithic valves and pumps presented in the first half of the thesis project were used for flow

control in this cytometry device due to their large scale integration property, which allowed additional functionality to be added in the future.

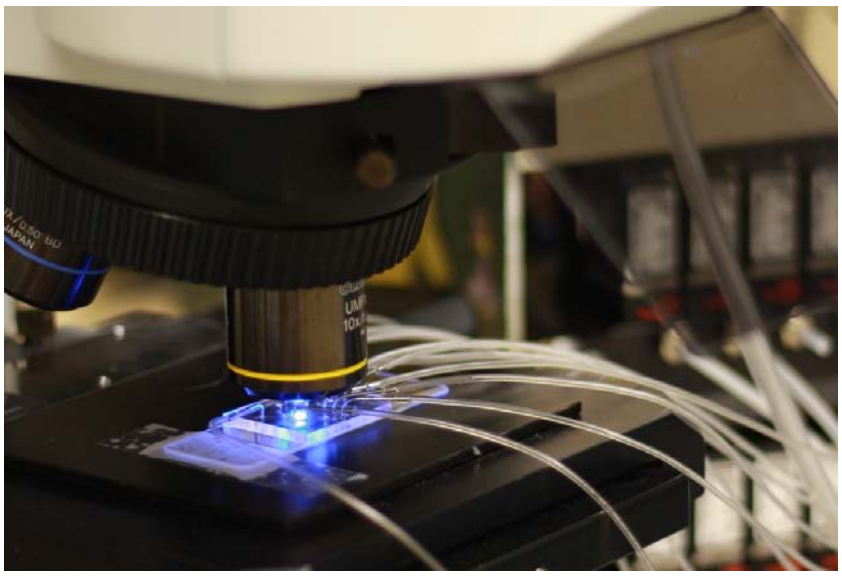

Figure 3 Image-based Microflow Cytometer with Integrated Pumps and Valves

Chapter 2. Materials and Equipment

This Chapter lists all the materials, chemicals, optical and electronic devices, as well as software packages used in this project. A description of each item and its relevance in this project is also presented.

2.1 Chemicals

PDMS (polydimethylsiloxane)

PDMS is among the top choices for microfluidic chip material because it is transparent, porous to gas, biocompatible, and soft with an adjustable elasticity. The Young's Modulus of PDMS is dependent on the ratio of the curing agent and the silicone base, and can be varied between 300 and 850 kPa. [Armani 1999] The low Young's Modulus allows large deflections of a PDMS membrane, making PDMS the perfect material for elastomeric valves.

In this project PDMS is used to make all the microfluidic microchips.

SU-8

SU-8 is a negative photoresist manufactured by MicroChem. It is currently the material of choice in the Waterloo Microfluidic Laboratory for photo lithography fabrication of channel molds. SU-8 is a photoresist that is capable of making features in a wide range of dimensions, has good adhesion to silicon wafer to withstand repeated use, is resistant to a variety of chemical solvent, and is hydrophobic in nature.

SU-8 is used to make all the control layer molds in this project.

AZ-50XT

AZ-50XT is a positive photoresist manufactured by AZ Electronics. This photoresist can be heated to reflow after its fabrication process to create semi-circular features. However, this photoresist has a limited range of dimensions (height between 15μm ~ 35μm were achieved in the author's laboratory) and poor adhesion to silicon wafer.

AZ-50XT is used to make all the flow layer molds in this project.

HDMS (Hexamethyldisilazane)

The surfaces of the silicon wafer oxidize very easily. The surface oxide forms long range hydrogen bonds with water adsorbed from the air. When the photoresist is spun onto such a surface, it adheres to the water vapor rather than to the surface, and poor adhesion results.

HMDS is used as a primer before spin coating that serves as an adhesion promoter for the AZ-50XT photoresist. 0.5~1 ml of HMDS is placed on and covers the entire silicon wafer, then spun until all the HMDS is evaporated before the start of the photo-lithography process.

Tridecafluoro-1,1,2,2-tetrahudroctyl Triethoxy Silane

This chemical is used at the very end of the photo lithography process to make the wafer surface hydrophobic. The coating method is vapour deposition. Place a few drops of the chemical in a vacuum dessicator along with the silicon wafer for over 20 min, the chemical will evaporate in the vacuum and deposit itself onto the silicon surface.

2.2 Biological Samples and Solutions

Yeast Cell and Culture

The W303 strain of yeast cells were used in this research. The following procedure was used for cell culturing: 1) frozen permanents are streaked out on media plates and incubated overnight at 37^{o}C until colonies are visible. 2) a single colony is picked from the plate using a sterile pipette tip and used to inoculate a 10 ml culture of liquid media. 3) incubate 10ml culture overnight until saturated. 4) Inoculate saturated culture into fresh liquid media. Incubate overnight, and then dilute in the YPD media to a concentration of approximate 10^{7} cells/mL. (The YPD media contains 1% Bacto Yeast extract, 2% Bacto Peptone and 2% glucose) This cell solution is agitated constantly using a magnetic stirrer during the experiments to keep the cells from clumping.

Polyethylene Glycol (PEG) Diacrylate

PEG Diacrylate is a bio-compatible polymer commonly used in lubricants. In this research it is added to the yeast cell culture media as a surfactant to prevent the cells from attaching to the microfluidic channel walls. It is chosen over other surfactants for its low toxicity. The user did not observe any adverse effects to the cells when PEG Diacrylate is added to the culture media.

2.3 Optical Setup

Olympus BX51M Microscope

The Olympus BX51M microscope is a metallurgical fluorescence, upright microscope with a blue excitation mirror unit (460-495 nm excitation filter, 505 nm dicrhoic, 510F nm emission filter), and a C-mount monochrome CCD camera (Photometrics CoolSNAP ES) with a maximum frame rate of 30fps. The objectives available are 10X and 50X magnification. It is used in this project whenever fluorescent particles are used.

This microscope uses reflective lighting, which is not ideal for visualizing yeast cells since the cells do not reflect much light. The cell images obtained from this microscope have very poor contrast. This microscope is also non-inverted, leaving only limited space between the chip and the objective for the connecting tubes.

Nikon Eclipse Ti Microscope

The Nikon eclipse Ti microscope is an inverted optical microscope with transmitted lighting. Both bright field and phase contrast techniques are available on this microscope. The objectives available on this microscope include 10X, 20X, and 40X magnification. This is the ideal microscope for cell visualization, and the inverted setup allows easy access to the microfluidic chip from above. A CCD camera from QImage is attached to the microscope, which has similar specifications as the CoolSNAP camera.

2.4 Other Equipment

Fluorescent Particles

Fluorescent particles were used as a substitute of yeast cells in several stages of this project since it is much easier to handle and visualize fluorescent particles than actual cells. The particles used were purchased from Molecular Probes, and they have a nominal diameter of 4.0 μm and peak excitation and emission wavelengths of 505 and 515 nm, respectively. The particle solution has a stock concentration of 2% or 5.7 x 10^8 particles/ml. These fluorescent particles tend to adhere to PDMS. Adding surfactant such as PEG Diacrylate will reduce the adhesion effect.

Fluorescent Dye

Fluorescent dye was used to visualize the sample and focusing fluid streams in the evaluation of flow focusing performances. The dye solution is a 1μM Fluorescein solution from Molecular Probes. It has a peak excitation frequency of 490nm and a peak emission frequency of 513nm.

Matlab

Matlab is a numerical computing environment that allows matrix manipulations, plotting of functions and data, implementation of algorithms and creation of user interfaces. Matlab was used for all the computational related portions of the project, including image acquisition from CCD cameras, image analysis, and classification. The image processing toolbox is heavily used.

PC

The computer used for the development of the image processing algorithm (cf. chapter 4) has an Intel Core 2 2.4GHz processor, 3GB of RAM and Windowx XP Professional SP3. Matlab was the sole software used on this computer for this research.

The computer used for controlling the flow cytometry process (cf. chapter 5) has a Pentium 4 3.6GHz CPU with 2GB of RAM, and Windows XP Professional SP3. Software and drivers used include Matlab 7.7, and μManager microscopy software.

Chapter 3. Elastomeric Membrane Structures and Microfluidic Large-Scale Integration

The definition of Microfluidic Large-Scale Integration (mLSI) is the fabrication of thousands of active microfluidic components, such as valves and pumps, on a single palm-size microchip, to allow direct and accurate control of fluid flow. Analogous to the electronic large scale integration, which has transistors as its building blocks, the building blocks of mLSI are the elastomeric membrane structures invented by Quake et al [Unger 2000]. This chapter presents an overview of the micro fabrication and operating principles of the various components, and then offers some guidelines for designing microchips utilizing the technology of mLSI. The details on how to set-up the mLSI control system is also documented in this chapter.

For step-by-step protocols of the fabrication processes, please refer to Appendix A.

3.1 Fabrication and Operation Principle

The building blocks of microfluidic Large Scale Integration (mLSI) are the monolithic microvalves (Quake's valve), which is consisted of an elastomeric membrane structure separating two microfluidic channels (Figure 4). To make the elastomeric membrane, a multi-layer structure is needed. The technology that enables the fabrication of such multi-layer structures is called multi-layer soft lithography (MSL). MSL is an extension of the popular fabrication technique soft lithography, which is described below.

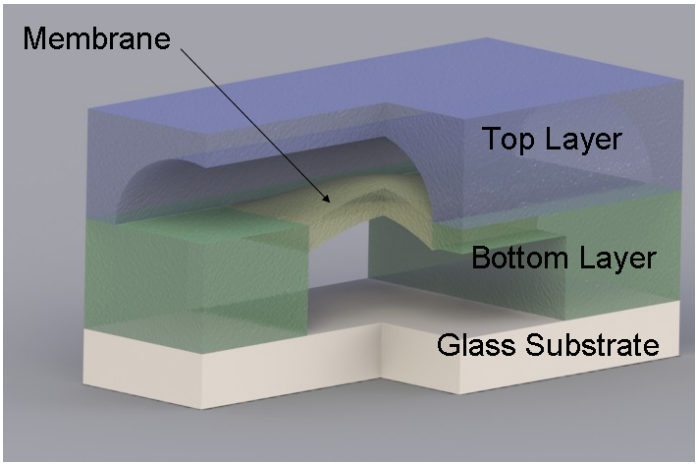

Figure 4 Section View of Membrane Structure

3.1.1 Regular and Multi-Layer Soft Lithography

Soft lithography is the technique of patterning an elastomer by curing on a micro-fabricated mold. It is one of the most common techniques to make microfluidic devices rapidly and inexpensively. The mold containing the design patterns can be fabricated in-house in less than 24 hr (fabrication described in 3.1.6), and a single mold can be used to cast hundreds of elastomeric chips. The elastomeric chip is made by pouring a mixture of a two-component curing system of a silicone polymer, polydimethylsiloxane (PDMS), with its curing agent onto the mold. After curing in the oven at 80°C, the elastomeric chip is peeled off from the mold and bonded to a glass cover slip.

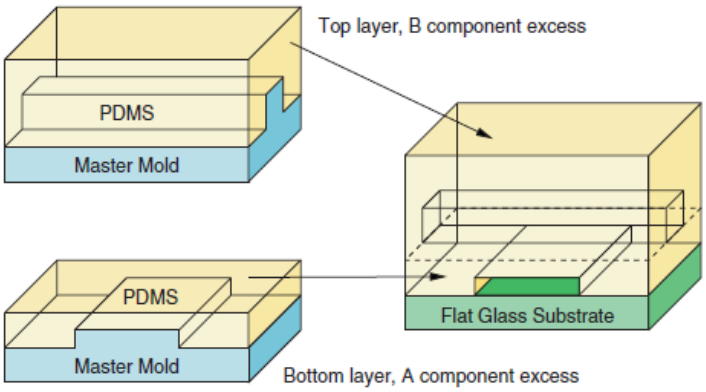

Figure 5 Fabrication Schematic of Multi-Layer Soft Lithography [Pandolfi 2008]

Multilayer soft lithography differs from regular soft lithography in its capability of bonding multiple patterned layers of elastomer. Multilayer structures are constructed by bonding two layers of PDMS each of which is separately cast from an individual mold, as shown in Figure 5. Usually, the bottom layer mold is spin-coated with PDMS to create a thin PDMS membrane on top of the features with a controllable thickness, while the thickness of the top layer PDMS is uncontrolled. After separately curing each layers, the upper layer is removed from its mold and placed on top of the lower layer, and cured further to cause the two layers to bond irreversibly. [Unger 2000] The above-mentioned elastomeric structures are formed at each crossing points between the top-layer channels and the bottom layer channels.

It is best to use different PDMS base to curing agent ratios for the two layers. The bottom layer should contain an excess of the PDMS base (base to curing agent ratio 20:1) for lower viscosity and ease of spin-coating, and the top layer should contain an excess of the curing agent (base to curing agent ratio 5:1) for quick hardening. The difference in chemical contents also results in better bonding between the layers.

The Waterloo Microfluidic Laboratory uses the Sylgard 184 brand of PDMS for fabrication, and its spin curve is illustrated in Figure 6. Most designs in this project used 1600rpm spin speed, which yield a PDMS thickness of around 55μm, or 15μm membrane thickness if the channels features on the mold are 40μm high. The baking times and temperatures for the two layers are critical to good fabrication quality. Incorrect settings can result in top layer being too

soft affecting feature dimensions, bottom layer too soft causing channel blockage, or layers too hard causing poor bonding between them. A complete and detailed protocol can be found in Appendix A.

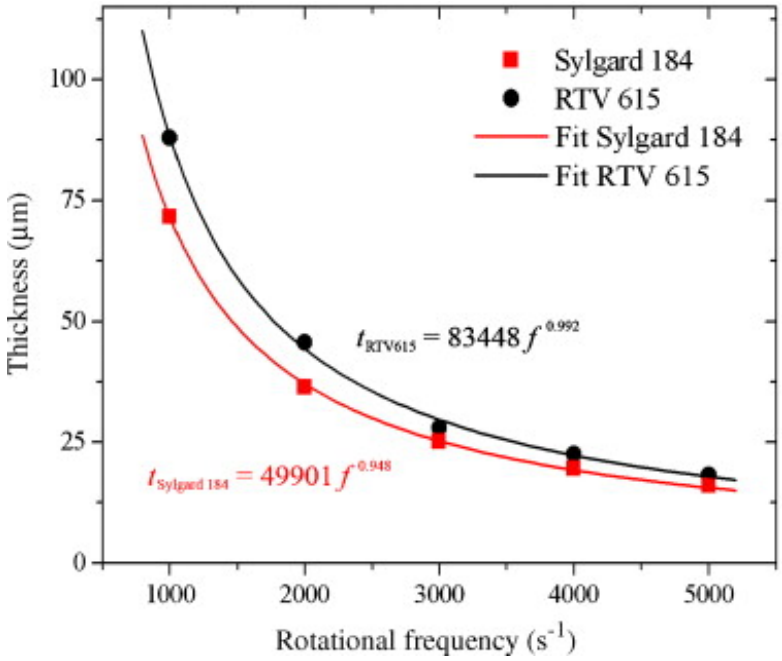

Figure 6 PDMS thickness at Different Spinning Speed [Armani 1999]

3.1.2 Microvalves

The elastomeric membrane structure can be used as a valve simply by applying pressure to channels on one of its two layers. The channel that is pressurized (referred to as control channel) deflects the membrane toward the other channel (referred to as flow channel, since it contains the working fluid), and seal the channel at this point. Changing the relative positions of the control and flow channels results in 3 variations of the valve, shown in Figure 7. Having the control channel on top of the flow channel creates the push-down valve. This type of valve allows the fluid layer to be bonded directly to the glass substrate, giving the user easier access to the fluid channel properties, and allows the PDMS portion to be peeled off and cleaned [Unger 2000]. The second variation has the control channel beneath the flow channel, called the push-up valve. A push-up valve gives users no access to the fluid channel once the chip is made, but requires much less pressure to activate, and can close higher aspect ratio flow channels comparing to a push-down valve [Kartalov 2007]. For complicated designs, one can also use both the push-up and push-down valves in the same chip for high valve density.

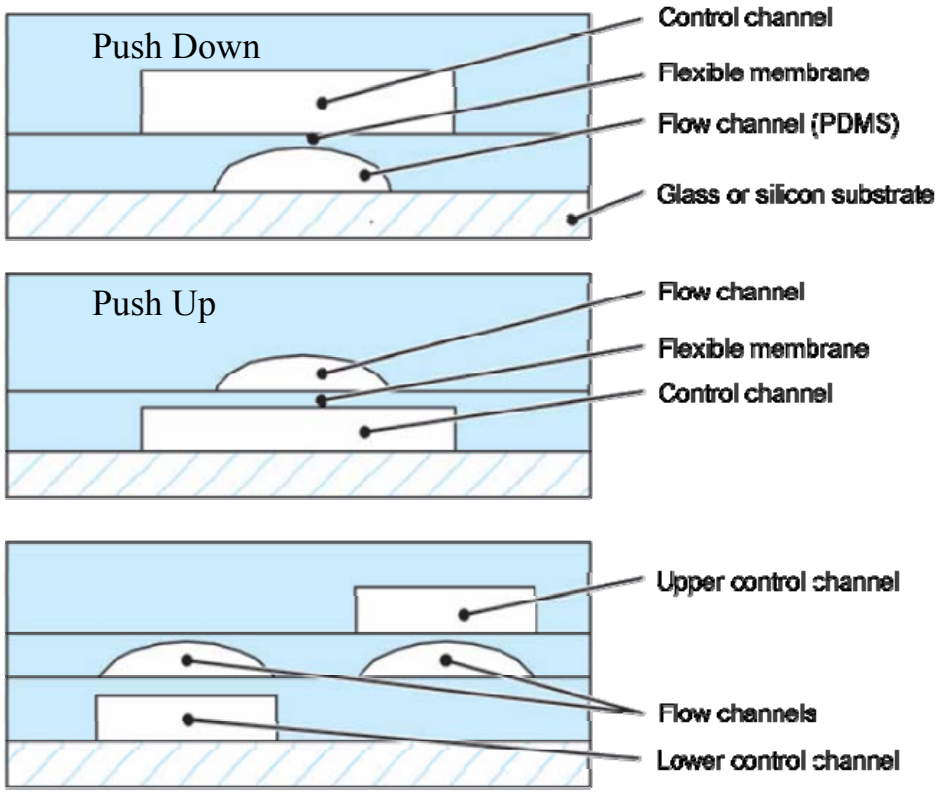

Figure 7 Different Valve Structures [Melin 2007]

For both the push-up and push-down valves, the flow channel must be semi-circular for the valve to seal completely.[Unger 2000] To make semi-circular channels, the photoresist AZ-50XT was used instead of SU-8. This photoresist can be heated to reflow after the fabrication process to created smooth semi-circular channels. Semi-circular channels also reduce the pressure required to close the valves.

3.1.3 Damper

The membrane structure can be used as a compliance device (fluidic damper) if no pressure is applied to the control channel. Any sudden change in pressure in the flow channel will cause the membrane to deflect to absorb/compensate for the change, effectively smoothing out the flow. The fabrication of dampers is identical to push-up valves except that no inlet is needed to apply a pressure, and the flow channel does not need to be semi-circular shape.

3.1.4 Peristaltic pump

A peristaltic pump can be fabricated from three valves arranged on a single channel and operated in a specific sequence. (Figure 8) The four steps in each sequence forms a peristaltic motion to propel the fluidic in the channel forward. The time between each actuation step is referred to as the pumping period. Under ideal conditions, the peristaltic sequence will propel fluid forward at a constant flow rate without any backflow, similar to a current source. However in reality, the valve opening/closing delay along with the downstream resistance will result in back flow, and occasionally complete failure of the pump.

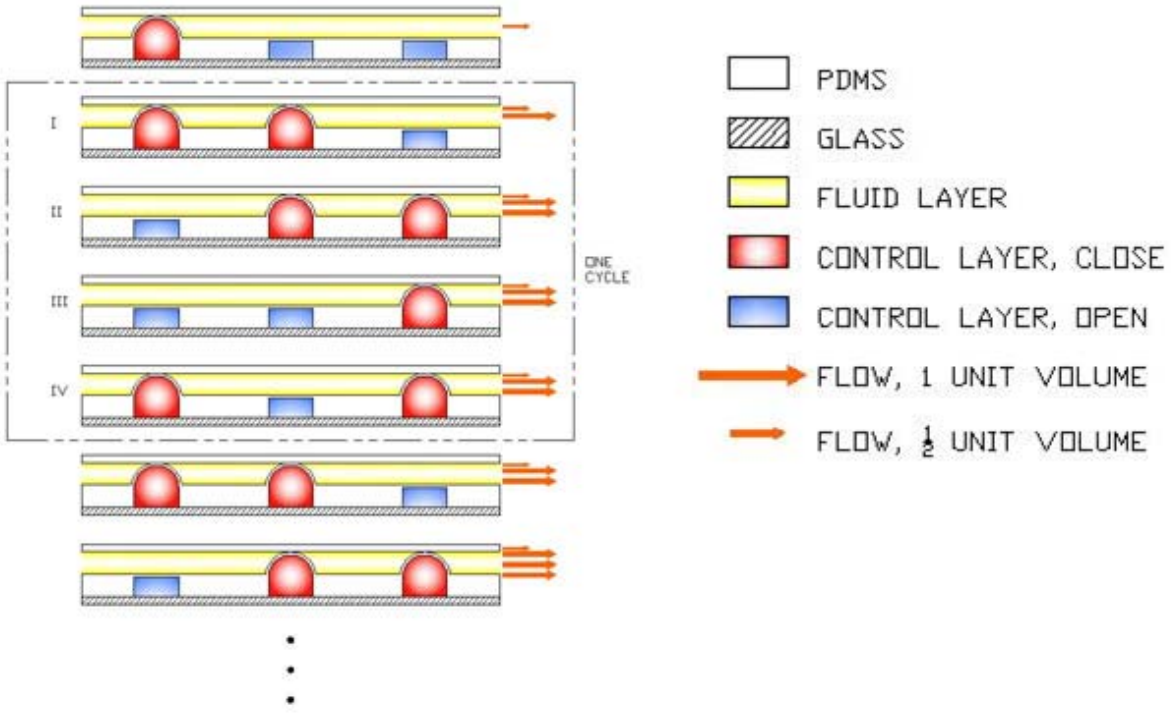

Figure 8 Working Principle of Peristaltic Pump

3.1.5 Large Scale Integration

The valve, damper, and pump mentioned above are relative basic components, many other microfluidic components could be created by combining them. An active mixer (Figure 9a) could be made by pumping fluid in a circular channel [Chou 2001]; a T-junction (Figure 9b) channel design could be used for metering precise amount of solution [Hong 2004]; a multiplexer (Figure 9c) could be created by fabricating control channels of varying widths [Thorsen 2002]. By utilizing many of these components, one could design stand-alone

chemical/biological analyzers with multiple functions and the capability of parallel processing on one single chip [Hong 2004; Marcus 2006]. Such a chip contains tens or hundreds of microvalves, yet the fabrication principle would be exactly the same, independent of design complexity.

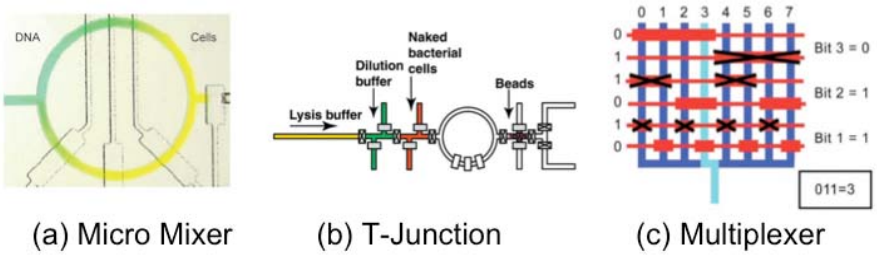

Figure 9 Higher Level Component [Thorsen 2002; Hong 2004; Marcus 2006]

3.1.6 Photo-Lithography

In the Waterloo Microfluidic Laboratory, the molds were patterned using a photolithography technique. Two different photoresists were used: SU-8 for square control channels, and AZ50XT for semi-circular fluidic channels. The fabrications for these two photoresists were mostly the same, except that they react to UV differently. SU-8 feature becomes permanent if exposed to light, but AZ50XT decomposes if exposed, as illustrated in Figure 10.

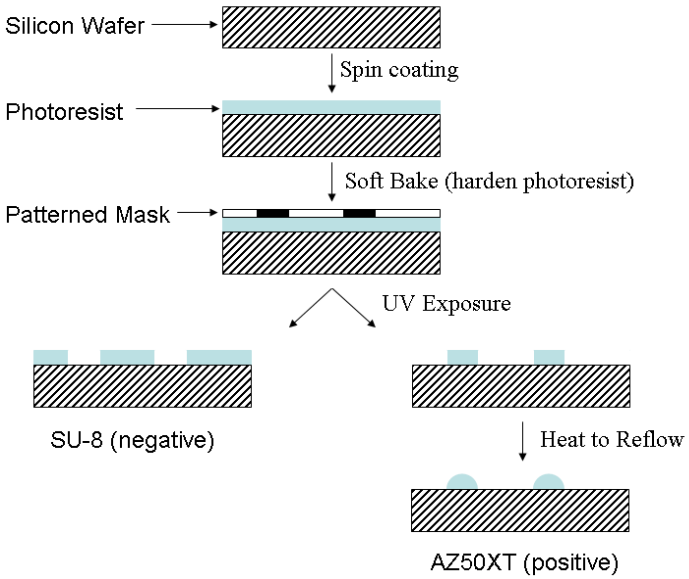

Figure 10 Procedure of Photo Lithography

First, the photoresist was spun on a silicon wafer to the desire thickness, then baked until harden, and exposed under UV with a high-resolution transparency film cover that contains the design pattern (referred to as mask). SU-8 is a negative photoresist, meaning the locations exposed to UV will undergo the cross-linking reaction and form a permanent structure, the AZ50XT is a positive photoresist, and thus completely opposite of the SU-8. After the exposure the wafer was dipped in a solvent solution (referred to ask developer) and the un-cross-linked photoresist is washed off, leaving the mold with only the desired features. For the SU-8 mold, this would be the last step of fabrication, which would leave the features square in shape with sharp edges. For AZ50XT mold, the mold was heated to above the photoresist's melting temperature, letting the feature flow into a semi-circular shape, then cooled down back to room temperature so the feature would be permanently rounded.

The SU-8 photoresist had been used in the UW Microfluidic Laboratory for the past four years and the protocols of fabrication had been well established. The AZ50XT however, was used for the first time. It was noticed by the author that, the AZ50XT is a very delicate photoresist that tend breaks off from the silicon wafer after repeated uses. The range of height it can achieve was also quite limited. Although the official documents claim it was possible to fabrication features with height up to 65μm, the author was only able to achieve a maximum height of ~40μm at a spin speed of 1000rpm. A list of different spin speed vs feature height is included in Appendix A.

3.2 Control Strategy

Although microvalves can be fabricated with high density on a single microfluidic chip, the control system needed to access each individual microvalve is massive and complicated. A controller unit (usually a PC) first sends out a signal to a relay circuit, the relay circuit in turn opens a pneumatic valve through a solenoid, the pneumatic valve then applies a pressure to the control channel on the microchip, which closes the valve and shuts down fluid flow in the flow channel. This connection is show in Figure 11 below.

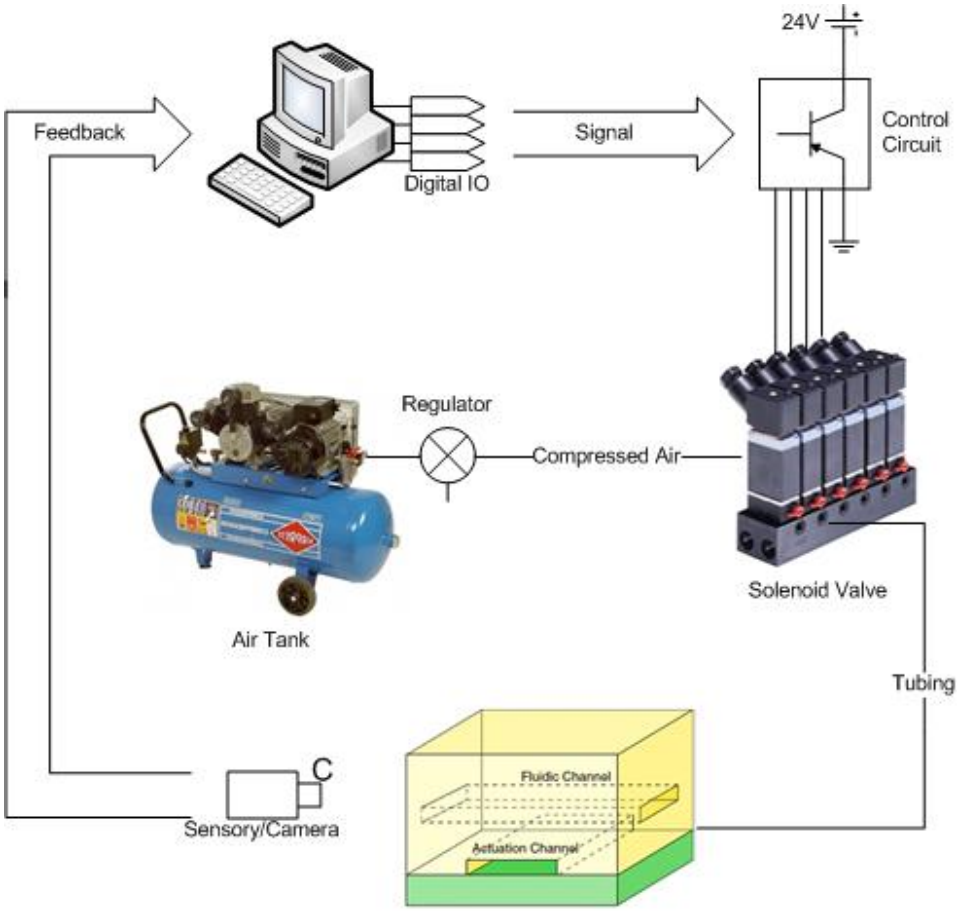

Figure 11 Connection Schematic of Valve Controller. The system includes: a solenoid valve array, a relay circuit, and a controller unit/PC.

3.2.1 Solenoid Valve Array

Since each solenoid valve is connected directly to one microvalve on the microfluidic chip, the control system will need as many macro-size valves as microvalves. For complicated devices, such as the mRNA analyzer developed by Marcus et al, it is common to have more than thirty microvalves [Marcus 2006], thus solenoid valves with small footprint are preferred. The solenoid valves will also be actuated repeatedly and over long period of time, thus valves with long service life need to be used. A 3-way direct acting rocker solenoid valve from Burkert Fluid Control Systems (type 6016) was chosen for its small size and long service life with low maintenance.

3.2.2 Relay Circuit

The Burkert solenoid valves have relatively low power consumption: each one is rated to draw 100 mA at 24V. However, when all forty valves are operated at the same time, up to 4 A will be drawn, which certainly cannot be handled by the controller unit directly. Thus a relay circuit is required to isolate the solenoid valves from the low-power controllers. The following circuit (Figure 12) was designed for this purpose.

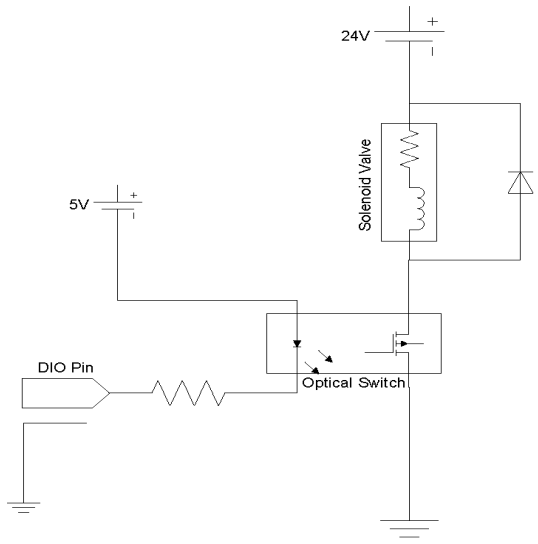

Figure 12 Relay Circuit for Solenoid Valve Control

An opto-isolator is used as the "relay" for its fast response and durability, as well as providing electrical isolation between the 5V control logic and 24V solenoid valve supplies. The TTL control output is setup as a current sink to handle the LED current through a current limiting resistor. The flyback diode parallel to the solenoid valve provides a current path to quickly dissipate current flowing in the solenoid coil when the valve is switched off. According to this scheme, two individual power supplies are required. One 24V, 120W voltage source is needed to power the solenoid valves. Another 5V power supply is shared by the controller unit and the optical relays.

3.2.3 Controller Unit

The purpose of the controller unit is to send the appropriate signals to the relay circuit to ensure smooth operations of the microvalves and pumps. The operation of the valves is straightforward: whenever a valve is required to close, the controller enables the digital I/O

(input/output) pin connected to that valve. For peristaltic pumping, the three valves are actuated by generating the output sequence of 110, 011, 001, 101, (Figure 8) where 0 and 1 indicate “valve open” and “valve close”, respectively. This sequence will pump the fluid to the right, one unit valve volume per cycle. Pumping in the opposite direction can be achieved by reversing the pumping sequence. The pumping speed can also be varied by either changing the time between the patterns, (changing pumping period/pumping frequency), or by adding a time delay between each cycle of patterns (cycle delay).

Using the data pins on a 25-pin parallel port available on a PC (shown in Figure 13a) is a simple way of controlling the valves. The parallel port has up to 12 output pins that could be used to connect to the microvalves, and can be programmed fairly easily. However, the number of output pins is severely limited, and the availability of parallel ports is decreasing significantly on newer computers, and thus the parallel connection can only be used for development purposes.

Peripheral digital input/output (DIO) boards can also be used. Figure 13b shows a 96 pin DIO board from CyberResearch. These boards provide up to 96 individual I/O pins, and are widely available. However, they have three major drawbacks that limit their user-friendliness. First, a DIO board usually needs its own driver installed on the PC, thus a PC will need to be dedicated to control the valves, and limit the adaptability of the device. Secondly, These DIO boards cannot be programmed internally, meaning the user must develop his/her own code. In the Waterloo Microfluidic Laboratory, VB, Matlab and Labview are all commonly used, thus three sets of function calls/vi’s must be developed. Thirdly, time sharing on Windows operating systems is not suitable for smooth pump actuation. For example, using Matlab to send a signal every 10 millisecond will result in signal periods varying between 5 ms to 20 ms. This uncertainty would affect the performance of peristaltic pumps.

(a) serial port (b) DIO module from CyberResearch (c) Renesas Microcontroller Kit

Figure 13 Different Choices of Controller Unit

Using a microcontroller dedicated for valve and pump control solves all the above problems. The microcontrollers today can have hundreds of digital I/O pins, built-in clock and timers, serial connection to PC, and interrupt handlers dedicated for real-time processes. Development kits (a Renesas dev kit shown in Figure 13c) are also available from the microcontroller manufacturers that have DIO headers, a serial port for communication with the PC, and an LCD display for easy debugging. The microcontroller can be pre-programmed to handle the pumping sequences to provide a user-friendly interface. The end user can then simply send high level commands to the controller via the serial/USB port from any PC to activate the desired valve/pump.

3.2.4 System Integration

The solenoid array, relay circuit, and the microcontroller are integrated together to produce a single stand-along microvalve controller unit. This unit is designed to be modular, enclosed and mobile. It is modular so the user can add or remove solenoid valves easily, enclosed so all the components are securely attached, and mobile so it can be move easily and shared by different users.

In total, forty solenoid valves were purchased along with five manifolds each capable of seating eight valves. A Renesas starter kit for the M32C/87 microcontroller was purchased. The microcontroller had a maximum operating frequency of 32MHz, had 16MB of address space, and 128 I/O pins available.

It was decided that every eight solenoid valves would be grouped into one module, since the I/O pins of the microcontroller were grouped and addressed in groups of eight. Each module

contained a square Lexan base, with the solenoid valve manifold mounted on one end, and a custom made electronic PCB (printed circuit board) attached at the other end. The PCB contained eight of the relay circuit described in the above section, a header for connecting to microcontroller IO pins, and another connector for power supplies. Five modules were made from the available equipment, but one was designated as a backup. An image of the module is shown in Figure 14.

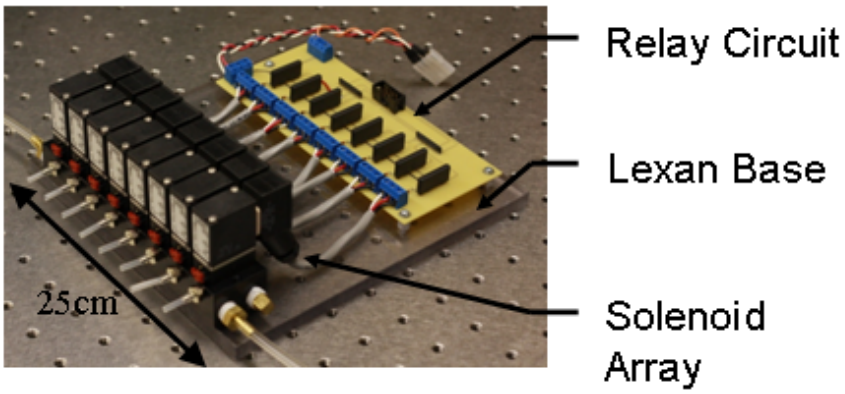

Figure 14 Solenoid Array Module

An aluminum enclosure (Figure 15) was made with the microcontroller and two power supplies mounted inside. One face of the enclosure was open with slots built-in to allow the valve modules to slide in and out. A pressure regulator with built in 5um air filter was located on the front face, and a fan was placed on the top of the enclosure for cooling of the solenoid valves during operation.

For the air pressure supply, a separate pressure tank was needed. To prepare for operation, a data cable from the microcontroller and a power cable from the 24V power supply was connected to the valve module, which was then slid into the enclosure (the module will sit firmly in the slot.) After all the necessary modules were plugged in, the pressure connection to each module was made in series using vinyl tubing. Then to operate the device, the user simply needed to connect the solenoid valves to the microfluidic chip using the appropriate tubing and connectors (recommended tubing and connector sizes are available in Appendix C), turn on the voltage and pressure sources, connect the PC to the enclosure via a serial cable, and command the valves and pumps by sending an 8-bit word from the PC using any desired computing software.

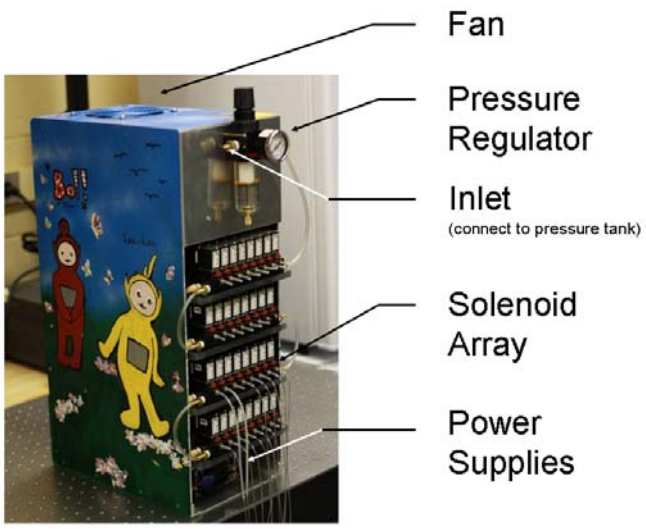

Figure 15 Control System Enclosure

3.2.5 Real Time Operating System

A real time operating system (OS) was programmed on the microcontroller. The operating system only had two processes, one for handling user inputs (input process), and a second for writing to the I/O pins to operate the valves (timer process). The two processes shared one piece of memory, which contained a sequence of values that represent the pattern of the pumps and the status of the valves. The input process had higher priority and can modify the data in the shared memory, and the timer process would only read from the shared memory and would not modify it.

The timer process would be called each time a timer interrupt occurs. The base timer period was set to 10 ms (100Hz). However the user could change the period dynamically to a maximum of 500 ms (2Hz). When the timer process was executed, it would read the next value on the sequence from the shared memory and wrote that value to the IO pins.

The user-to-controller communication was setup via asynchronous serial communication. When the user sends command information (an 8-bit command word) from the PC serial port, an interrupt would be generated in the controller OS, which would in turn call the input process. The input process would decode the information form the PC and then update the share memory accordingly: if valves/pumps were turned on by the user, the corresponding port

values would be added to the sequence; to turn off any valves/pumps, the corresponding port values would be subtracted.

The operating system kept track of all valves and pumps by assigning ID's to them. The solenoid valves on each module were numbered 0 to 7 (000 to 111 in binary) from left to right, the modules were also numbered 0 to 3 (00 to 11). When multiple modules were used, the module number was added to the front of the individual valve ID. For example, the 3rd valve (010) on the second module (01) would have an ID of 01010 in the OS. For pump operation, the first six valves on each module were designated for use as two pumps and numbered 0 and 1. The overall numbering was similar for valves: pump ID 101 refers to the second pump (1) on the third module (10). This numbering system allowed easy communication between the users to the controller. To access the valves/pumps, the user needed to send an 8-bit word via the PC serial port, this word would be coded using the following rule (Figure 16):

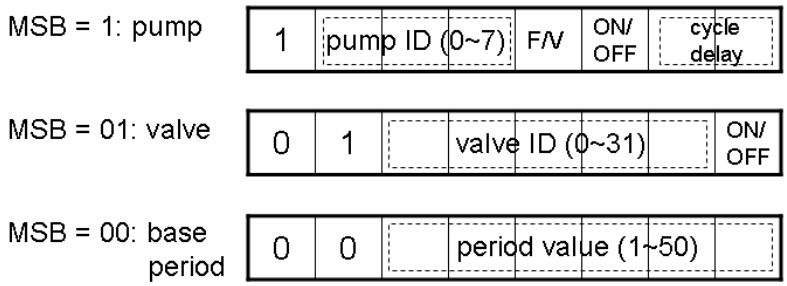

Figure 16 Coding scheme of serial communication

The command word could take on three different types of meanings: to command a pump, to command a valve, or to change base period. The most significant bit (MSB) of the word represented whether the word is to command a pump. In the pump case, the next three bits (bit 2, 3, 4) represent the ID of the pump, bit 5 indicates whether the pump was to work in the forward or reverse scheme, bit 6 indicates the on/off state of the pump, and bits 7 and 8 represent the cycle delay: "00" – no cycle delay (full pumping speed), "01" – one cycle delay between each pattern cycle (half speed), "10" – three cycles delay between each pattern cycle (quarter speed), "11" – 7 cycles delay between each pattern cycle (one-eighth speed).

If the most significant bit is equal to 0, then the second bit represents whether the word was for commanding a valve, or for changing the base period. If the second bit is 1 then the word was for commanding a valve, and the next five bits represent the valve ID, while the least significant bit indicates the on/off status of this valve.

If the first two bits are 00, then the word is meant for changing the base pumping period. The decimal value of the word, between 1 and 50, is the new base period in multiples of 10ms, i.e. a value of 1 means a base period of 10ms, and 50 means a base period of 500 ms. Decimal values of 0 and 51 to 63 have no meaning.

The above is the complete description of the micro valve controller system. Design documents, such as printed circuit board (PCB) layout, and pseudo code of the OS can be found in Appendix B. The next section will be focused on mLSI again, and look at the rules and cautions involving the design of mLSI components.

3.3 Design Guidelines

Many parameters – such as size, channel dimensions, actuation pressure, and pumping frequency – needed to be considered when designing the valves and pumps in an integrated microfluidic circuit. Understanding the relation between fundamental physical parameters and device performance would be a key step in the development of design guidelines for these microfluidic devices [Studer 2004]. However, most of the device performances/design rules reported in previous studies was based on empirical observations, while theoretical or numerical analyses had only been reported in a handful of published studies. This was mainly due to the difficulty of experimental validation of the theoretical/numerical results. Measuring displacement and velocity in the micro environment is challenging, and the current micro fabrication techniques for PDMS microchip also have low repeatability. Thus, this research did not aim to investigate the underlying physics of the elastomeric membrane structures. The design guidelines provided in this section are mostly based on the author's experience and observations, as well as the work of other scholars in this area.

3.3.1 Analytical Model of Membrane

The deflection membrane is the fundamental structure of any mLSI device, and its physics had been extensively studied. A numerical analysis was reported by Pandolfi et al, for exploring microvalve designs. This was a very detailed study that considered nonlinear material properties, non-smooth contact, and the swelling of PDMS, but requires heavy computing power [Pandolfi 2008]. Kartalov et al, reported a method of analyzing the elastomeric valves by approximating them as beams [Kartalov 2007], which significantly reduced the complicity at the cost of accuracy. The analytical model recommended by the author is a plane-strain approximation illustrated by J. P. Landers [Landers 2008].

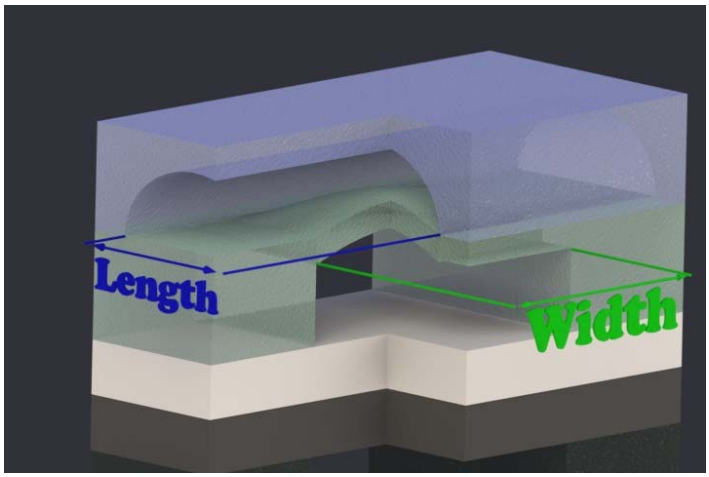

Figure 17 Schematic of Membrane Structure. The deciding parameters of the membrane are its length, width, and thickness

The model makes the following assumptions: 1) the length of the membrane (L, control channel width, shown in Figure 17) is at least two times larger than the width (w, fluidic channel width), so the variation in deflection along the length can be ignored – plane-strain assumption. 2) the width of the membrane (w) is ten times the membrane thickness (t), and 3) the deflection of the membrane is more than the membrane thickness, to satisfy the large deformation membrane behaviour assumption, in which the centreline stretch of the membrane dominates bending. If all the assumptions are satisfied, then the maximum membrane deflection (δ_{max}) is:

$$\delta_{\max} = \frac{w}{4}\left(\frac{3Pw}{\bar{E}t}\right)^{\frac{1}{3}} \tag{3-1}$$

Where P is the applied pressure to the membrane, $\bar{E} = E/(1-v)^2$ is the plane-strain modulus, and v is the Poisson's ratio for the material. The volume under the deflection membrane V is approximately:

$$V \approx \frac{2Lw\delta_{\max}}{3} \tag{3-2}$$

Since the fluidic channel has a semi-circular cross section, while the deflection of the membrane is parabolic, thus the pressure required to seal a fluidic channel of height h is slightly more than the pressure need to deflect the membrane by h:

$$P_{seal} \geq \frac{\bar{E}t}{3w}\left(\frac{4h}{w}\right)^3 \tag{3-3}$$

The closing pressures of the valve for different valve dimensions are experimentally verified in the next section.

3.3.2 Valve closing pressure

Closing pressure is defined as the pressure required to completely seal a stagnant flow channel. A set of experiments was conducted to measure the closing pressure for valves with varying width and length. A chip with a grid of valves was made, with fluidic channel height of 20μm, membrane thickness of 20μm, the control channels' widths varying between 100 and 250μm, and the fluidic channels' widths varying between 50 and 150μm. The control layer was filled with DI water while the flow layer has air in the channels. This setup allowed the operator to clearly observe the closing and opening of the valves, while reduced delays in the pressure system. (In all future experiments the control channels are always filled with water. This is possible because PDMS is porous to gas, pressurized water will force out the air originally in the control channel and fill the channel easily.) The pressure in the control layer was increased slowly by adjusting the pressure regulator at the source of the compressed air to a maximum of 200kPa, and the closing pressure for each valve on the grid was recorded.

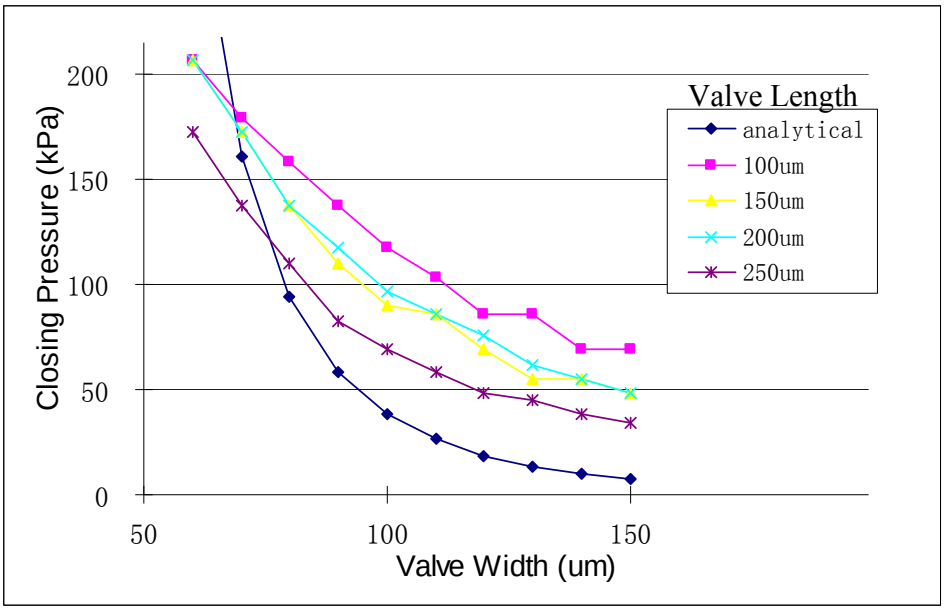

Figure 18 Experimental and Analytical Closing Pressure for Different Valve Lengths (Please note: pressures equal to 200kPa was not enough to close valves with width less than 60μm)

Figure 18 showed the plot of the experimental results along with the analytical closing pressure calculated using formula 3-3. The material parameters used were: E = 300kPa, ν=0.45. The analytical formula for calculating closing pressure was independent of valve length because the length is assumed to be at least two times larger than the width to satisfy the plane-strain condition. However, the valve length had an effect on the closing pressure, as shown by the experimental results. As the valve length decreased, higher pressure was needed to close the valve, which was expected since as the valve length decreased, the system deviated from the plane-strain assumption, and the stretching of the membrane along the length would affect the closing pressure. Also, the experimental closing pressures did not increase as sharply as those calculated analytically when valve width increased. This was also expected since as the valve width increased, the model again deviated from the plane-strain assumption.

The fluidic channel height and membrane thickness were both chosen as 20μm for this experiment because these dimensions allow for the most efficient fabrication procedure. Too low a channel height would make the bonding between the fluidic layer and control layer difficult due to possible collapse of the channel, while too thin of a membrane is prone to leakage (membrane thickness is dependent on the spin-coating of PDMS). Note that 10μm

membranes are also quite durable, and require much less pressure to close, due to time limitation the closing pressures for 10µm valves were not tested. Thus, the experiment showed that for these parameters, the valve width (fluidic channel width) should be at least 60µm. If the width of the valve was less than 60µm, the closing pressure increased dramatically. This property could be used to the designers' advantage and allow control channels to cross flow channels without creating a valve to reach flow channels in a complicated chip design.

Although some consistency can be found between the analytical and experimental values, it should be pointed out that the micro-fabrication process is not precise enough to produce accurate and repeatable device dimensions. The property of the material, PDMS, also can vary significantly between different patches of fabrication. Thus the analytical model can only be used as a crude estimate when designing valves.

3.3.3 Damping coefficient estimation

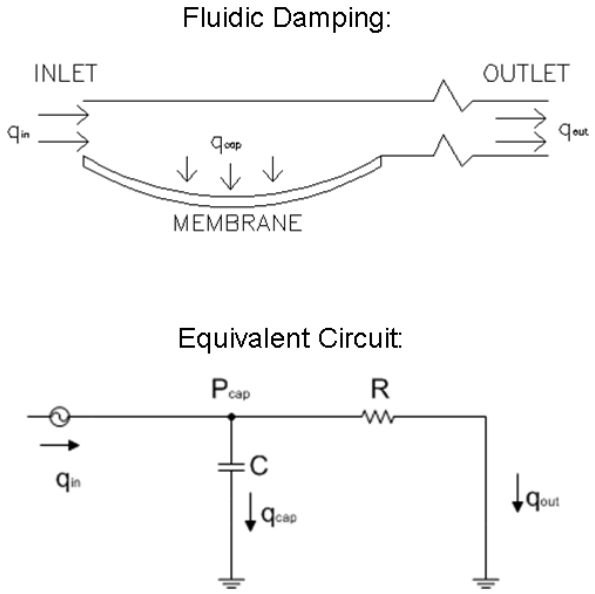

Figure 19 Fluidic damping and the equivalent electrical circuit.
(P – pressure, q – flow rate, R – hydraulic resistance, C – capacitance)

Any feature of the fluidic network whose internal volume changes with pressure acts as a fluidic capacitor, because those volume changes imply that additional mass will be "stored" inside the feature. A free-deflecting membrane has the above mentioned property and thus can

be considered as a capacitor. The fluidic capacitor can be modeled as a circuit capacitor element and build a low-pass filter that can damp out the disturbances in the fluidic channel.

Figure 19 showed the setup of a typical fluidic damper: a fluidic channel, with a deflecting membrane and a hydraulic resistance. When excess flow comes from upstream of the membrane, the membrane will deflect downward to store some of the excess flow, and slowly release it afterwards. This fluidic setup could be modelled using lumped circuit elements. The excess flow from upstream could be viewed as a variable current source, and the membrane as a capacitor that is parallel connected to ground with a resistor that represents the hydraulic resistance of the downstream channel. The input of the system is the upstream current q_{in}, and the output is the downstream current q_{out}. This lumped model assumed that the downstream channel is an ideal resistor that has no compliance. The upstream current is assumed as a current source because of the nature of the peristaltic pump. An ideal peristaltic pump will allow current flow in one direction only at a pre-defined rate, acting similar to an ideal current source. Applying KCL:

$$q_{in} = q_{out} + q_{cap} \tag{3-4}$$

Where $q_{cap} = C\frac{dP_{cap}}{dt}$, in which $P_{cap} = Rq_{out}$. Substituting these in equation 3-4, this becomes:

$$q_{in} = q_{out} + RC\frac{d}{dt}q_{out} \tag{3-5}$$

Now expressions for R and C needed to be found. The channel resistance can be estimated using the following empirical formula for laminar flow in a rectangular microchannel:

$$R = \frac{12\mu L}{wh^3(1-0.63h/w)} \tag{3-6}$$

Where μ is the viscosity of the fluid, L, w, h are the length, width and height of the microchannel respectively. Note the hydraulic resistance was assumed to be independent of the flow rate inside the channel.

The governing equation for the capacitor is:

$$q = C\frac{dP}{dt} \tag{3-7}$$

Where q is the flow rate, C is the capacitance, and P is the pressure across the capacitor. The flow rate across a capacitor is also the instantaneous change of the fluidic volume under the deflecting membrane:

$$q = \frac{dV}{dt} = \frac{dV}{dP}\frac{dP}{dt} \tag{3-8}$$

Equating 3-7 and 3-8, the capacitance C = *dV/dP*. The volume *V* under the deflecting membrane is given in equation 3-2, which is a function of the maximum deflection $\delta_{max,}$ and δ_{max} is a function of the pressure over the membrane:

$$C(P) = \frac{dV(P)}{dP} = \frac{d}{dP}\left(\frac{1}{6}Lw^2\left(\frac{3wP}{\overline{E}t}\right)^{1/3}\right) = \frac{Lw^2}{18}\left(\frac{3w}{\overline{E}t}\right)^{\frac{1}{3}}P^{-\frac{2}{3}} \tag{3-9}$$

Or $C(P) = C_0(P)^{-\frac{2}{3}}$, where $C_0 = \frac{Lw^2}{18}\left(\frac{3w}{\overline{E}t}\right)^{\frac{1}{3}}$. Note the capacitance is a function of *P*, the pressure cross the capacitor. Now substitute 3-9 and 3-6 into 3-5 to get an ODE that relates the input current q_{in} to the out output current q_{out}:

$$q_{in} = q_{out} + RC_0(P)^{-\frac{2}{3}}\frac{d}{dt}q_{out} = q_{out} + RC_0(Rq_{out})^{-\frac{2}{3}}\frac{d}{dt}q_{out}$$

$$q_{in} = q_{out} + Dq_{out}^{-\frac{2}{3}}\frac{d}{dt}q_{out} \tag{3-10}$$

Note equation 3-10 is a non-linear ordinary differential equation due to the $q_{out}^{-\frac{2}{3}}$ term. The equation can be linearized by approximating this term using the average of the input current:

$$q_{in} = q_{out} + D\overline{q}_{in}^{-\frac{2}{3}}\frac{d}{dt}q_{out} \qquad (\overline{q}_{in} \text{ is the time average of } q_{in}) \tag{3-11}$$

Equation 3-11 represents a linear first order low pass filter. The frequency response of such a system will attenuate signals at high frequency while leave low frequency signals unchanged. The cut-off frequency of the system is the frequency at which a signal's power is attenuated by 50%, and can be estimated by:

$$f_C = \frac{1}{2\pi D\overline{q}_{in}^{-\frac{2}{3}}} \text{ [Hz]} \tag{3-12}$$

The purpose of the fluidic damping system was to attenuate the flow pulsing effect generated by a peristaltic pump. The pulsing effect would have a frequency equal to the frequency at

which the peristaltic pump operates. Thus when designing a damper, its cut-off frequency should be the same or higher than the operating frequency of the pump. With this criteria, the channel dimensions and the damper sizes can be designed accordingly.

3.3.4 Pump performance

Pumping requires dynamic actuation of the microvalves, thus the response time would become a limiting factor in pumping. Studies by Quake's group on the original microvalve had shown that the membrane deflects rather quickly with opening/closing times of less than 15 ms (75Hz bandwidth) [Unger 2000]. The same study also showed that the flow rate achieved by the pump increases linearly with the pumping frequency (decrease with pumping period) to a maximum of 2.35 nL/s at ~ 75Hz (Figure 20), roughly equal to the maximum actuation speed of the microvalve. Above this rate, increasing numbers of pump cycles would compete with incomplete valve opening and closing, and thus effect the pumping performance.

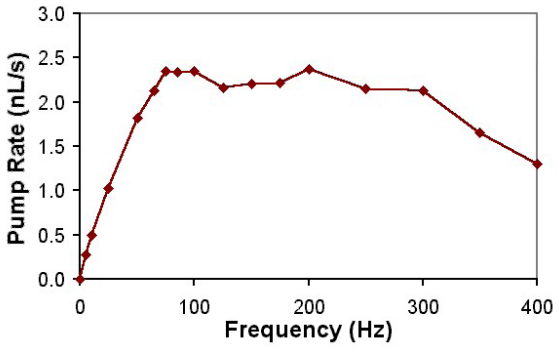

Figure 20 Pumping rate of a peristaltic micropump versus various driving frequencies.[Unger 2000]

The above result was for 100µm x 100µm x 10µm (length, width, membrane thickness) valve dimension, and 50 kPa applied air pressure. Pumping rates were determined by measuring the distance traveled by a column of water in thin tubing (0.5 mm inner diameter)[Unger 2000]. Note that for such small flow rates, this method of measurement is very crude.

The pumping flow rate can also be estimated analytically. Since for every pumping cycle, one unit of valve volume is propelled (recall section 3.2.3), and there are four patterns in each pumping cycle, thus the flow rate should be:

$$Q_{pump} = \frac{V_{valve}}{4 \cdot \left(1 / f_{pump}\right)} \qquad (3\text{-}1)$$

Where Q , V and f are the for flow rate, volume, and frequency, respectively. Applying this formula to Unger's data results in a flow rate of Q_{pump} = 1.3nL/s, which is in the same order of magnitude as the measured flow rate. This suggested that formula 3-1 can be used to provide a rough estimate of the pump flow rate.

A problem with these peristaltic pumps would be the pulse waves generated by the pumping cycles. This problem could be alleviated by adding dampers downstream from the pumps [Fu 2002]. However, dampers would also act as a pressure source, adding unnecessary load to the pumps and affecting the flow generated by the pump. The author had observed a sharp decrease in flow speed across a damper. Thus designers should be cautious when using dampers combined with peristaltic pumps. The best way to avoid pulsing was to operate the pump at high frequencies. It was observed that, for pumping frequencies greater than 20Hz, the compliance of the PDMS channel itself was enough to smooth the flow.

3.3.5 Fabrication Considerations

As mentioned earlier, it is difficult to achieve precise dimension using the existing fabrication procedure and material. However, some cautions could improve the accuracy and repeatability of the micro fabrication.

Shrinking of PDMS

Liquid PDMS cures on the silicon mold at a temperature of 80C. When the PDMS chip is peeled off the mold at room temperature, the thermal stress will cause the PDMS to shrink. This affects both the feature dimensions, as well as the alignment of fluidic and control layers. Thus when printing the photo-mask for fabrication, the following two rules should be followed:

1. Major features, such as alignment markers, on the top layer must be scaled by 1.015 (1.5%) to compensate for shrinking.

2. Minor features, such as channels with width less than 100μm, should be enlarged by 10μm. Features 20μm or less should be avoided as much as possible.

Control Reservoir Spacing

The control reservoirs were pressurized to a maximum possible pressure of 200kPa, poor bonding between the control layer to the glass substrate would fail under such pressure and cause leakage. Thus, the control channel reservoirs, where pressure connectors are attached, must be 1mm apart to prevent leakage between the reservoirs.

Other Cautions

Below is a list of rules/cautions one should consider when designing and operating microfluidic systems with integrated valves. Some are a recap of rules mentioned earlier.

1. The channel height for the semi-circular fluidic layer should be more than 10μm to prevent the sticking of channel to the membrane during bonding.
2. The fluidic channel reservoirs must be free of air bubbles to ensure proper operation of the pump. Observations show that the pumping speed changes significantly if the channel contains two-phase fluid.

3.4 Conclusions

This chapter documented the detailed information needed to set up a microfluidic large scale integration (mLSI) system. The theoretical knowledge of the fabrication techniques, including photo-lithography, soft-lithography, and MSL were introduced. The structure of the microvalve, the operation of valves and pumps were also illustrated. Following them was a complete description of the external control system, which described the equipment choices, system integration, and programming of the control system. Design guidelines of the valves, dampers, and pumps were given in the last part of the chapter, which were derived from analytical modelling and experimental observations. The content of this chapter should be sufficient to serve as a guide for anyone looking to develop a similar system in the future.

Chapter 4. Cell Cycle Identification using Image Processing

Yeast cells, or Saccharomyces cerevisiae, are commonly used in biology as a model species to study cell cycles. One of the many reasons of its popularity is that, yeast cell cycle progression is easily monitored by changes in the cell shape, allowing researchers to easily identify cells in different phases of its life cycle. The second project of my thesis work – the content of chapter 4 and 5 – is focused on developing an automated flow cytometer capable of identifying and sorting yeast cells in different cell cycle phases. In this chapter I will steer away from micro fabrication and hardware design, and take a look at the development of an image based pattern recognition algorithm.

This chapter contains the design and testing of the algorithm using only stationary cells. The application of this algorithm to flow cytometry is the topic of chapter 5.

4.1 Background

Several image-based yeast cell morphology identification devices/algorithms have been described previously. Koschwanez et al. reported a fiber-optic bundle imaging device, capable of identifying a budding and non-budding yeast cell [Koschwanez 2004]. The device does not require a microscope but cannot extract any information on bud size, thus the classifier cannot distinguish between cells in the S-phase and M-phase. Ohtani et al. developed an image processing program (called CalMorph) that can extract quantitative information on cell morphology such as cell size, roundness, and bud neck position, etc., however this is limited to fluorescent stained microscopic images [Ohtani 2004]. There are also several microfluidic devices for yeast cell imaging mentioned in the literature. Lee et al. reported a microfluidic chip with a passive filtering-and-trapping mechanism that is capable of fixing cells in the same focal plane for imageing without any moving components on chip [Lee 2008]. Ohnuki et al. developed an active cell trapping mechanism that uses flexible PDMS membranes to hold cells stationary and in the same focal plane [Ohnuki 2009]. However, both designs lack the ability to isolate or manipulate single yeast cells.

Despite the advancements in image analysis, to the best of the authors' knowledge there has not been any attempt to combine pattern recognition and image processing for the classification of yeast cells in different life cycle phases. Supervised pattern recognition methods have become increasingly popular in biomedical imaging studies. For example, pattern recognition has been successfully applied in the identification of ovarian cancer from confocal microendoscope images [Srivastava 2008], classification of Listeria colonies from light-scatter patterns [Bayraktar 2006], recognition of biological microorganisms using digital holography [Moon 2006], and detection of lesions in computer tomography (CT) [Bazzani 2001; Gokturk 2001]. The classification of yeast cell cycle phases is also a very good application for supervised machine learning, as training data can be easily obtained from the vast database already developed for yeast cell morphology.

In this project an image-based machine learning algorithm is reported which is not dependent on fluorescent staining. The algorithm analyzes non-fluorescent microscopic images of

stationary yeast cells, extracts morphological features from the cells, and classifies the cells into the most-fitting cell cycle phases based on the information that it was trained on previously. This algorithm is intended for implementation in a microfluidic chip involving cell studies; it must therefore account for all the constraints and special circumstances in a microfluidic channel environment, such as high and uneven background noise and blurring due to rotation and drifting.

The details of the design and experimentation of the algorithm is explained in sections 4.2 to 4.5 below. Section 4.2 describes the methods for cell harvesting and data collection. Section 4.3 introduces an image enhancement and segmentation algorithm that first eliminates background noise and improves the contrast of the microscopic cell images, then applies threshold and extracts geometrical information from the images. In section 4.4 the appropriate features are selected and three machine-learning classifiers are chosen, and in section 4.5 the performance of the image analysis algorithm and the classifiers under different conditions are studied.

4.2 Methods

The W303 strain of yeast cells was used to collect stationary images of cells used as training data, the procedure is outlined below.

A drop of the cell culture media was placed on a glass slide and observed using the Olympus BX51 microscope with a 50X/0.5 objective that has a depth of field of 1μm. Images of the cells were captured using a CCD camera interfaced with ImagePro software as 8-bit TIFF and later converted to type double in Matlab. The exposure time was set to 90ms for regular cell images. One image with no-cells in the viewing area was taken to serve as the background reference image. 100x100 pixel image clips containing only one cell (referred to as cell-clip) were cropped from the raw images to form a data set, and for each cell-clip, a same-size image clip was cropped at the same location from the background image. This clip (background-clip) serves as an estimation of the true background of the cell-clip. In total, 240 stationary cell-clips were collected. Each of these cell-clips were labelled according to the relative size of its bud as class 1 (phase G1: no bud), class 2 (phase S: small bud), and class 3 (phases G2/M: large bud).

4.3 Image Processing Algorithms

The main goal of the image processing algorithm is to extract statistical features from the cell images in order to classify cells in different division phases. In the previous work on image detection of the yeast cell cycle, the first step is usually a threshold technique that isolates the cell areas from the background [Koschwanez 2004; Ohtani 2004; Niemisto 2007]. This step converts the original grey-level image into a binary image that helps distinguish the cell shape from the background. The accuracy of this conversion is critical to the performance of the entire classification algorithm. It should be able to obtain a completely enclosed shape that preserves the original contour of the cell shape, and thus dilation and erosion must be avoided as much as possible, since dilating and eroding pixels around the shape will erase the fine details.

4.3.1 Image Enhancement Sub-Algorithm

Otsu's method [Otsu 1979] is based on finding a threshold value that maximizes the separation between darker pixels (cell boundaries) and brighter pixels (background and cell interior) which is then used for cell clip segmentation. Otsu's method is available as a built-in function of Matlab, and its performance on the cell clips is shown in Figure 21. However, as seen in Figure 21, there is significant background noise, and the segmentation results in an un-closed (horseshoe shaped) cell boundary.

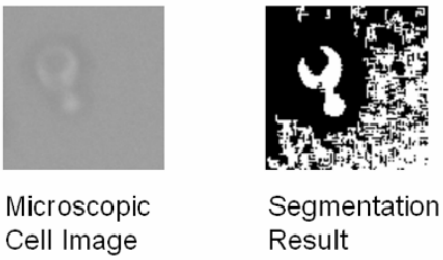

Figure 21 Otsu's segmentation method

The primary issue we have found with this approach is that it limits the categorization to only two levels, although there are three distinctive clusters in each cell-clip: background, cell boundary, and cell interior. Thus an algorithm that clusters the image according to these three groups should be more effective at segmenting cell-clips.

Typical bright field microscopic images have very low contrast, high noise, and uneven background lighting compare to fluorescence images, and it is usually difficult to infer these three clusters from the image histogram, as is evident from Figure 22a. However, since the statistical information of the background is available, an image enhancement algorithm is developed that uses the prior knowledge of the background to improve the contrast between the background, cell boundary, and cell interior, effectively clustering the image into three clusters.

The first step of the algorithm is to obtain the statistical information of the background. A background-clip of the same size is cropped from the same location as the cell-clip which ensures the background-clip has the same illumination distribution as the cell-clip. The background-clip is averaged using a 20x20 mask to produce a background-mean matrix: μ_{bg}, and the variance of each 20x20 region is also computed to form a variance matrix: σ_{bg}^2 of the background. Then for the intensity of each pixel in the image, its Generalized Euclidean Distance (GED) to the background mean is computed:

$$GED_{i,j} = \frac{p_{i,j} - \mu_{bg-i,j}}{\sigma_{bg-i,j}}, \forall i, j \tag{4-1}$$

where $p_{i,j}$ is the grey level of the pixel at index (i, j). Then a mapping function is applied to each pixel's GED to map it to a new value GED' using equation (4-2):

$$\begin{cases} GED'_{i,j} = \left(\frac{GED_{i,j}}{n} \right)^3, & \left| GED_{i,j} \right| < n \\ GED'_{i,j} = A_X \times GED_{i,j}, & \left| GED_{i,j} \right| \geq n \end{cases}, \forall i, j \tag{4-2}$$

where n is a threshold value and A_X is an amplification factor. This mapping function maps all pixels with GED less than n closer to zero, while it amplifies the pixels with GED greater than n further away from n. The value of n can significantly alter the image segmentation process described in the next sub section: smaller values of n result in a thicker cell boundary but with more noise, while larger values of n create thinner cell boundaries and less noise. The preferred values for the amplification factor A_X and threshold n were both determined heuristically to be 20 and 0.8 respectively.

Now the mapped GED values can be converted back to pixel values. The pixels with GED equal to zero are assigned a pixel intensity of 0.5 instead of the original background intensity, while the background variances were used to compute the intensities of other pixels. Any intensity value greater than one or less than zero is assigned a value of one and zero respectively:

$$p'_{i,j} = GED'_{i,j} \cdot \sigma_{bg-i,j} + 0.5 \quad p'_{i,j} \in (0,1) \quad \forall i, j \tag{4-3}$$

Figure 22b shows a cell-clip after applying the enhancement algorithm and its histogram. It is obvious that the enhanced clips have lower noise, and the contrast is significantly improved as the background, cell boundary, and cell interiors have intensities of 0.5, 0, and 1 respectively.

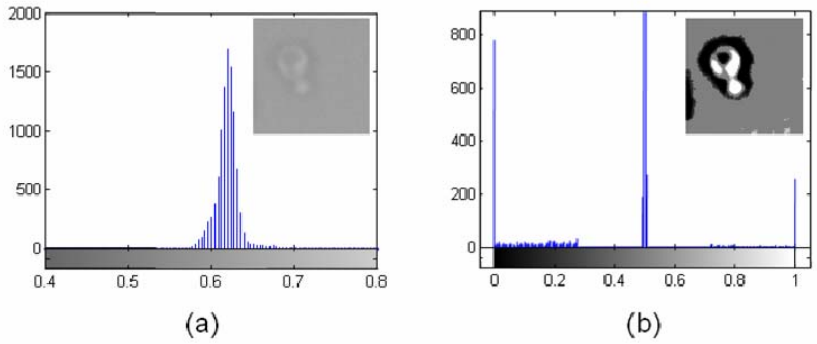

Figure 22 (a) Cell clip and histogram prior to enhancement. (b) Enhanced cell clip and histogram

4.3.2 Shape Identification Sub-Algorithm

By observing the enhanced cell-clips, it was noted that the bright cell interior is a good representation of the shape, but often the cell interior is divided into several pieces, such as shown in Figure 22b. Obtaining a completely enclosed cell shape from the bright interior region would require many repetitions of pixel dilation and erosion, which is not ideal due to the changes in the size of the interior boundary. The interior edge of the dark cell boundary also represents the shape of the cell very well, but such an edge may not exist if the cell boundary does not close completely, for example the clip in Figure 23(1). An enclosed cell shape can be obtained by finding a method that can connect and close an open boundary. Thus the shape identification algorithm is created based on obtaining the inner edge of the dark cell membrane, and is outlined in Figure 23:

1)	Starting with the original enhanced image	
2)	First apply a threshold at 0.3 to the enhanced image. This creates a binary image, *bw,* representing the dark cell boundary cluster.	
3)	Apply eight-neighbour dilation to *bw*. It was found heuristically that 10-pixel dilation is sufficient to close any open cell boundaries.	
4)	All holes in the shape are filled, followed by 10-pixel erosion. Resulting in a closed blob approximately representing the original shape of the cell.	
5)	The edge pixels of this blob are obtained.	
6)	The edge pixels are super-imposed onto the original binary image *bw* (obtained at step 2) to obtain a completely closed shape of the cell boundary.	
7)	The shape of the inner edge of the cell boundary is obtained.	

Figure 23 Steps of Image Segmentation

4.3.3 Feature Extraction Sub-Algorithm

With the cell shapes successfully extracted from the original images, it is now possible to extract specific features from the shapes to classify between cells in different cell division phases. Traditionally, the manual classification of yeast cells generally uses the following guidelines: first determine whether a bud exists; if not, the cell is classified as belonging to the G1 phase. If a bud is detected, the size of the bud is examined to determine whether the cell is in the S phase (characterized by a visible but small bud), M phase (characterized by a very

large “bud”, usually the same size as the parent cell), or G2 phase (bud size in between the S and M phases). The automated classifier will also follow this guideline, thus features must be extracted from the cell images that can reflect the shape and bud size of the cells.

The major difference between budding and non-budding cells is their shape: non-budding cells look like compacted circles while budding cells have a peanut-like shape. Thus the compactness and axis ratios should be capable of reflecting these differences.

The compactness is a geometric feature that is measured by the ratio of its area to its perimeter squared [Theodoridis 1999]:

$$c = \frac{A}{p^2} \tag{4-4}$$

where the area A and perimeter p can be measured using Matlab’s binary region analysis tools. A non-budding cell should have a lower compactness measurement while a budding cell will have a higher compactness measurement.

The axis ratio is the ratio of the shape’s major axis to its minor axis. Both can be obtained using Matlab’s binary region analysis tool. A non-budding cell, looking more like a circle, will have an axis ratio closer to 1, while cells with larger buds will have larger axis ratios.

To extract the bud size feature from the cell shapes, the bud must be isolated from the parent cell. One existing method of bud separation is to traverse through the boundary of the cell shape and look for convex boundaries that represent the location of the bud neck. [Ohtani 2004] This method is very efficient at finding the bud neck, however its accuracy cannot be guaranteed because a convex section of the boundary may not necessarily be the bud neck (an example is shown in Figure 30 in section 4.5). The proposed bud isolation algorithm assumes the parent cell to be circular and tries to locate it using circle detection techniques. First the area of the cell shape A_c is determined (in pixels), and then its equivalent radius is calculated as $\sqrt{A_c}/\pi$ rounded up to an integer (pixel) value. A circular mask of the same radius is then created and slid across all the pixels that belong to the cell shape to find the location where the mask best matches the cell shape. All the pixels that are covered by the circular mask are then

removed, and the remaining pixels represent the bud. Then the bud-to-area ratio feature can be obtained by dividing the size of the bud in pixels to the size of the entire cell.

Of the three features mentioned above, the axis ratio and compactness can be obtained with the shortest time, while bud ratio is the most difficult feature to obtain.

4.4 Feature Spaces and Classifiers

All of the 240 stationary cell-clips were enhanced and segmented using the image process algorithm described in the section above. Three features – axis ratio, compactness, and bud-to-area ratio – were extracted, and the sample means and variances for each class in each feature space were computed. The histograms of the distributions in these feature spaces along with a Gaussian distribution of the same sample means and variances are plotted in Figure 24 to Figure 26. The 2D distributions in the compactness-axis ratio space and in the bud ratio-compactness space are plotted in Figure 27 and Figure 28.

The following observations can be made from these figures:

1. The three classes are roughly Gaussian in shape, but are not linearly separable in any feature spaces.
2. Class 1 (no bud) has the most compact class shape in any feature space, while classes 2 and 3 tend to be more scattered with more outliers.
3. In all feature spaces, some data points from class 2 and 3 are consistently found in the region of class 1. Their buds were lost during the image segmentation process.
4. Some cells in class 1 were identified with large bud ratio and/or axis ratio, because these cells have elongated ellipsoidal shapes, possibly due to the stirring of the cell solution stretched the cells.
5. The axis ratio and compactness features both show good separation of class 1 from the rest of the classes, but not good separation between class 2 and 3, especially for axis ratio.
6. The bud ratio feature has better separation (least over lap) between classes 2 and 3.

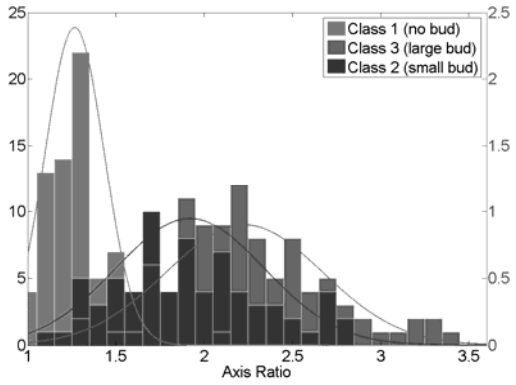

Figure 24 Class distributions in Axis Ratio Feature Space

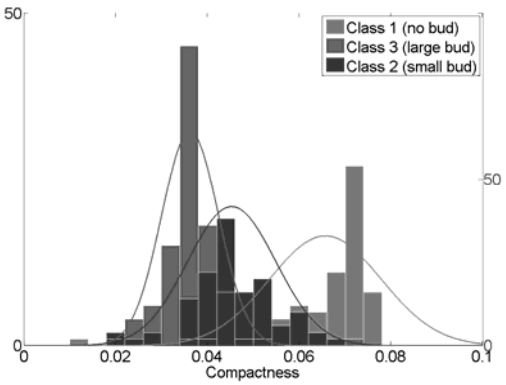

Figure 25 Class distributions in Compactness Feature Space

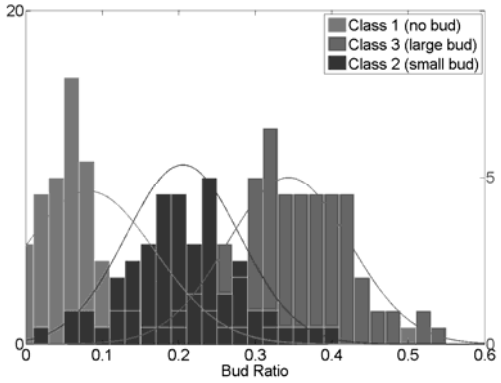

Figure 26 Class distributions in Bud Ratio Feature Space

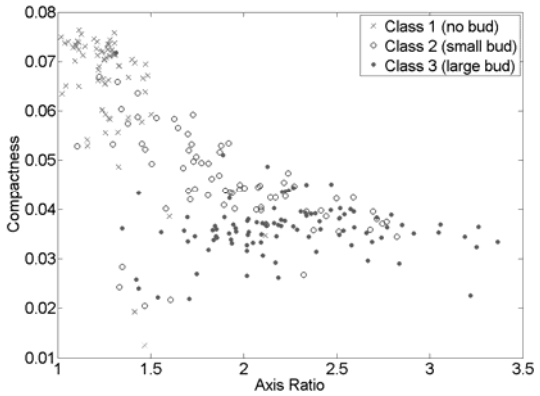

Figure 27 Class distributions in Compactness-Axis Ratio Feature Space

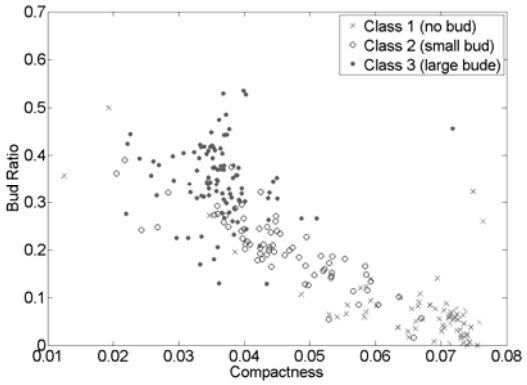

Figure 28 Class distributions in Bud Ratio-Compactness Feature Space

As mentioned earlier, the automated classifier will have two sequential steps: first classify between budding and non-budding cells (isolate class 1), then classify between small bud and larger bud cells (distinguish class 2 & class 3). The histograms suggest that the bud ratio feature can be used to classify between classes 2 and 3 with good accuracy, while axis ratio and compactness can only be used for classification between classes 1 and 2. Based on this information, three different feature sets are proposed. Set #1 uses only single features (1-Dimensional feature spaces) for classification: it uses compactness to classify between class 1 cells from the rest of the classes, and bud size to classify between class 2 cells and class 3 cells. Set #2 uses two features (2-D feature spaces) simultaneously: axis ratio and compactness together for class 1, and compactness and bud size together to classify between classes 2 and 3. In set #3 all three features are used for classification between the three classes (3-D feature space).

Three classification methods are also proposed: the Mahalanobis distance classification, k^{th} nearest neighbour (kNN), and linear-kernel support vector machine (SVM). The Mahalanobis distance classifier is a parametric classification method that is only accurate if the classes are Gaussian in shape[Theodoridis 1999]. The linear-kernel SVM tries to find a linear discriminant that best separates two classes; it is the most computationally efficient of the three but also requires the classes to be non-convex for accurate classification. kNN is a non-parametric classifier that assigns a sample to the class of its k^{th} closest training data point [Devijver 1982]. It applies to any class shape, but is computationally inefficient.

4.5 Performances

In this section the performance of various components of the image based classification algorithm were evaluated, so the optimal parameters could be chosen and the limitations of the algorithm can be understood.

4.5.1 Image Enhancement

Threshold Parameter

As mentioned in section 3.1, the threshold value *n* in equation (2) had a critical role in the entire algorithm. The value of *n* represented the cut-off value between the background noise and cell features, and the effect of various values of *n* was show in Figure 29 below:

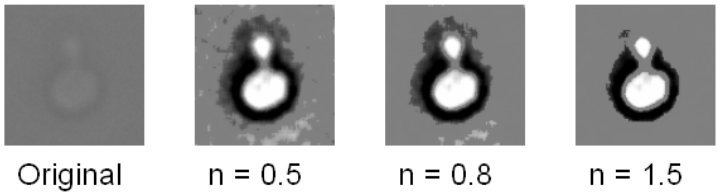

Figure 29 Enhancement Result for different threshold value n

As *n* increased, more background noise was eliminated by the enhancement algorithm, and the edge of the cell membrane became sharper. However, a high *n* value resulted in un-closed cell membrane boundaries, and subsequently the failure to extract features from the image since the segmentation algorithm only tried to find the inner edge of the cell membrane. A low *n* value would also result in incorrect features due to background noise.

Table 1 Comparison of Image Segmentation Performance for Different n Values

n	Fail to extract feature	Class variances in compactness feature space [x10^{-4}]		
		Class 1	Class 2	Class 3
0.5	0	6.17	2.22	6.38
0.8	1	0.77	0.78	0.37
1	5	1.09	0.83	0.41
1.5	23	1.43	0.83	1.47

An experiment was conducted where the image enhancement and segmentation algorithm was applied to the entire set of cell clips with different values of *n*. The resulting classification performance was tabulated in Table 1. The second column of the table showed the number of clips (out of 240) that failed to return a cell shape. The last three columns presented the variances of the three classes in the compactness feature space. $n = 0.8$ had the smallest class variances, meaning there was the least number of outliers, thus $n = 0.8$ was chosen as the optimal threshold value.

Segmentation and Bud Isolation

Figure 30 showed the result of the segmentation and bud isolation on several cell-clips. In general the segmented shapes closely represented the actual cell shape, although the bud sizes were slightly enlarged due to the segmentation algorithm. The segmentation algorithm was not

completely fail-proof: an image with a very large gap (4th clip in Figure 29) in the cell boundary could not be closed completely, thus resulting in the algorithm returning an empty shape. The bud isolation algorithm over estimated the size of the parent cell, which resulted in an under estimation of the bud size. This was introduced purposely to try to negate the enlargement of the bud during the segmentation process, and to make sure that small defects on the boundary are not identified as buds.

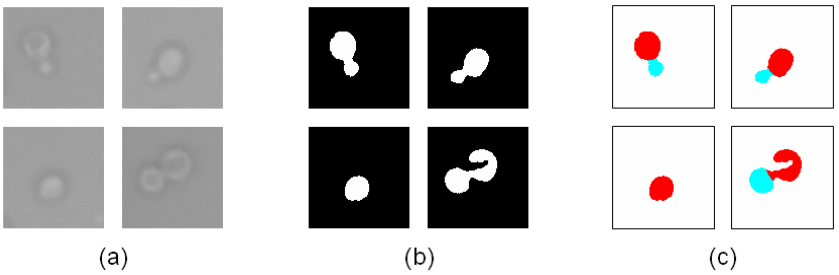

Figure 30 Examples of Cell Clips. (a) Original Images. (b) Segmented Images. (c) Bud Separation Result

Computational Complexity

The entire algorithm was coded in Matlab using as many built-in image analysis functions as possible. On average, for each 100x100 cell clip, the image enhancement algorithm needed a computational time of 10ms per clip, the image segmentation algorithm needed 90ms per clip, and the feature extraction algorithm needed 50ms per clip, of which 40ms was dedicated to the bud isolation process. Thus a total of 150ms was needed to perform all the image analysis and feature extract procedures.

4.5.2 Optimal Feature Space and Classifier

For each classification method, half of the 240 original cell clips were randomly chosen to form a training set, and the classifier was obtained using the training set. Then the classifier was used to classify the remaining half of the samples, the results of which were compared with the actual class labels. Each classifier was tested ten times in each set of feature spaces by selecting ten random training and testing sets from the original data set. The confusion matrices were shown in Table 2-Table 4 below

Table 2 Confusion Matrices for Classifiers using Feature set 1

		Classifier Results								
		Mahalanobis			SVM			kNN (k=3)		
		1	**2**	**3**	**1**	**2**	**3**	**1**	**2**	**3**
Actual Class	**1**	93%	4%	4%	79%	11%	11%	87%	7%	7%
	2	29%	49%	22%	12%	69%	19%	13%	72%	15%
	3	2%	11%	87%	1%	15%	84%	1%	10%	89%

1-D feature spaces: class 1 - compactness; class 2 & 3 - bud size

Table 3 Confusion Matrices for Classifiers using Feature set 2

		Classifier Results								
		Mahalanobis			SVM			kNN (k=3)		
		1	**2**	**3**	**1**	**2**	**3**	**1**	**2**	**3**
Actual Class	**1**	94%	3%	3%	95%	3%	3%	91%	4%	4%
	2	14%	64%	21%	12%	66%	22%	13%	74%	14%
	3	1%	10%	89%	1%	15%	83%	1%	8%	91%

2-D feature spaces: class 1 - axis ratio & compactness; class 2 & 3 - compactness & bud size

Table 4 Confusion Matrices for Classifiers using Feature set 3

		Classifier Results								
		Mahalanobis			SVM			kNN (k=3)		
		1	**2**	**3**	**1**	**2**	**3**	**1**	**2**	**3**
Actual Class	**1**	97%	2%	2%	94%	3%	3%	84%	8%	8%
	2	16%	57%	28%	13%	64%	23%	7%	81%	12%
	3	0%	8%	92%	1%	14%	84%	1%	13%	86%

3-D feature space: axis ratio, compactness & bud size

The performance for different feature sets showed that set 2 resulted in the most accurate classification. Set 1 was inaccurate because it is 1-D in nature, making it difficult to separate over-lapping classes. Set 3 resulted in similar accuracy as set 2 except for the kNN classifier.

The performance of different classifiers showed that the Mahalanobis distance method was very accurate at classifying samples in class 1 and class 3 in any feature space, but miss-classified many of the class 2 samples. This was mainly due to the inaccuracy in the covariance estimation of the classifier. Since class 1 and class 3 had more outliers compared to class 2, the estimated covariance of class 1 and class 3 would be significantly greater than class 2, resulting in significantly biased class boundaries. This is evident in Figure 24 to Figure 26.

The support vector machine classifier was less prone to outliers compared to the Mahalanobis distance method. It could also accurately classify samples in class 1 if having 2 or more features, could classify class 2 samples more correctly. However, it was still inaccurate when classifying between class 2 and 3. This was expected because these two classes have major overlaps, thus a linear classifier could not achieve good performance.

kNN was the most accurate classifier overall. Unlike the two other classifiers, kNN could classify samples in all three classes with good accuracy. For samples in class 2, kNN could achieve an accuracy of 74% accuracy in feature set 2 (2-D feature space), while maintaining 90% accuracy for class 1 and 3. The high performance of kNN in compactness-bud size feature space was due to the distribution of class 2 and 3 in the compactness & bud ratio feature space. As shown in Figure 10, class 2 had a long and narrow shape, while class 3 was scattered around class 2. This type of distribution could not be linearly separated, and could not be approximated using Gaussian models, hence the poor performances of SVM and Mahalanobis distance. Since kNN did not assume any class/boundary shape, it can accurately classify between the two.

However, the performance of kNN droped slightly for feature set #3, when all three features are considered. It was difficult to visualize the class distribution in 3D, but a possible reason could be that there were more outliers in the 3D feature space that impacted the performance of the kNN classifer.

Table 5 Computational Speeds of Different Classifiers

	Classification time (per sample)
Mahalanobis	2ms
SVM	0.7ms
kNN (k=3)	20ms

Table 5 showed the computational speeds of each classifier algorithm, not including the image analysis. Although kNN required a much longer time (20ms) to make the classification decision compared to SVM and Mahalanobis distance, it would not be the bottleneck of the entire image analysis system, since the image enhancement and segmentation required much

longer computational time. Thus, the k^{th} nearest neighbour (kNN) classification method with k = 3 was the most accurate and consistent classifier. Feature set 2, which used the axis ratio & compactness feature space, and compactness & bud size second feature space sequentially, were the optimal feature spaces for this application.

4.5.3 System Performance under Different Conditions

Effect of intensity

In addition to the original set of cell clips, another set of clips were taken with half the exposure setting as the original, as shown in Figure 31

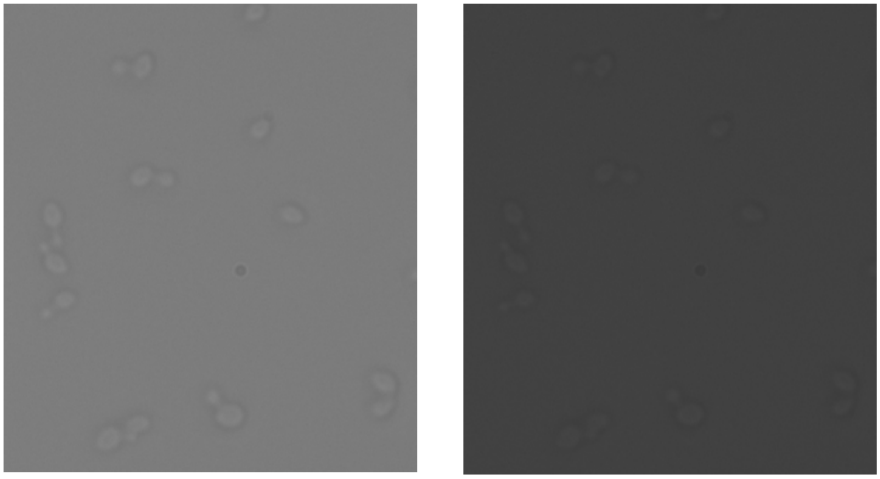

Figure 31 Cell Images under Different Exposure Setting

The image enhancement and segmentation algorithms were performed on these clips with the same parameters, and then classified using the kNN classifier obtained using the original clips as the training set. A comparison of the image enhancement results for full exposure and half exposure settings was shown in Figure 32, and the performance of the algorithms for half exposure setting were shown in Table 6:

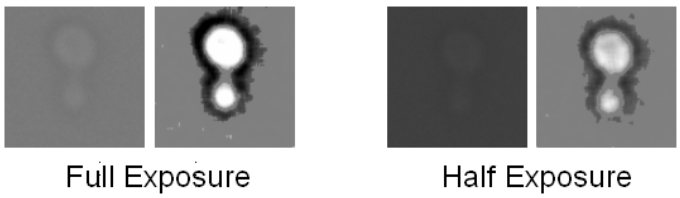

Figure 32 Image Enhancement under Different Exposure

It was noticed that the enhanced image under half exposure conditions had lower contrast compared to the fully exposed image, since the un-enhanced image already had lower contrast due to insufficient exposure.

Table 6 Performance of Algorithm under Half Exposure Setting

Fail to extract feature	Class variances in compactness feature space [x10^{-4}]					kNN Results Class		
	Class 1	Class 2	Class 3			1	2	3
0	0.29	1.47	0.75	Actual Class	1	71%	29%	0%
					2	13%	42%	46%
					3	8%	17%	75%

Although at the low exposure setting, the cell images had lower contrast and high noise ratio, the image enhancement and segmentation algorithms were able to extract meaningful features from the cell clips, shown by the low class variances. The kNN classification accuracy was lower than for the properly exposed images, with the most inaccuracies for class 2 cells. These observations showed that the higher signal to noise ratio of the low exposure setting had a negative impact on the performance of the system.

Effect of focusing

Figure 33 Appearance of Cells under Different Focal Setting

Due to the ellipsoidal shape and refractive index difference between the cell content and surrounding liquid media, yeast cells act similarly to convex lenses and have significantly different appearance when observed in-focus and out-of-focus. [Bittner 1998] The original cell

images were taken with the microscope lens focused near the foci of the cells (about 10 μm from the actual cell position), resulting in the bright spot in the middle of the cell. [Bittner 1998] This focus setting was referred to as standard focus, and had many optical advantages. It resulted in bigger cell sizes, more circular cell shape, and higher contrast between the cells and the background. To test the performance of the imaging algorithms under different focusing conditions, two more sets of cell clips were taken. One set was taken at 5μm further away from the cell (over focus), and the second set was taken with the microscope focused on the cell (under focus, 10μm from the original focal plane) resulting in the images shown in Figure 33.

The over-focused cells generally looked larger than the original, especially the buds. The cell membranes also looked more blurry. The image enhancement and segmentation algorithms both worked with these images. However, the bud information was lost due to blurred images, as shown in the confusion matrix in Table 7. The kNN classifier was still capable of distinguishing budding and non-budding cells, but it failed to find any cells with small buds.

Table 7 Performances for Over Focused Images

		kNN Results		
		1	**2**	**3**
Actual Class	**1**	3	0	0
	2	1	0	1
	3	0	0	5

The under-focused cells looked darker, and did not show a bright interior spot. This appearance was different to the standard focused cells. The image enhancement algorithm could still improve the contrast of the cell clips, shown in Figure 34, but the image segmentation algorithm, which tried to find an interior boundary of the darker regions, failed completely. However, the enhanced images could easily be segmented using a different algorithm. Then the feature extraction and classification algorithms could still be used for under focused cells.

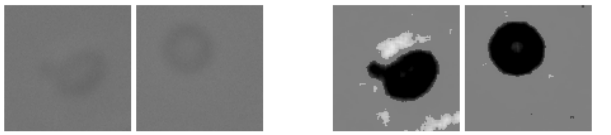

Figure 34 Enhancement Result for Under Focused Images

4.5.4 System Performance with Different Microscope

Recall the cell images were all collected using the Olympus BX51 microscope, which would not be commonly used for yeast cell visualization, but rather for fluorescent microscopy (due to the unavailability of the Nikon Ti microscope, the initial development was done using the Olympus BX51). However, after completing the development process, the classification system was tested using cell images taken with the Nikon eclipse Ti microscope.

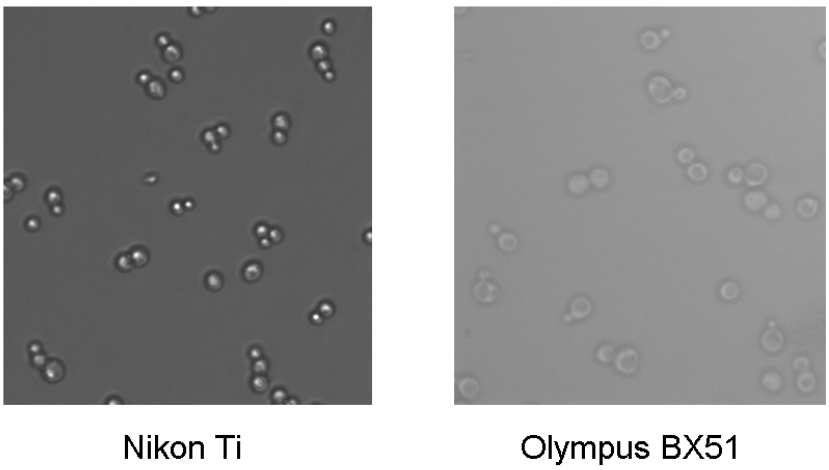

Figure 35 Cell Images from the Nikon Microscope and the Olympus Microscope

Figure 35 showed the images taken from the Nikon microscope compared to the Olympus microscope. The magnification on the Nikon microscope was 30X (20X objective with a 1.5X internal multiplier) compared to 50X on the Olympus, thus the cells appeared slightly smaller. The image from the Nikon microscope was significantly sharper compared to that from the Olympus, and the shutter speed was also much faster (10ms for Olympus, 300μs for Nikon) due to the transmitted lighting condition. The good image quality yielded good performance of the image processing algorithm. Smaller cell size and higher contrast also resulted in significant faster processing speed: feature extraction took only 25ms instead of 140ms.

However, to classify cells accurately, new training data needed to be obtained with the Nikon microscope. This showed that the algorithm is capable of working with different microscope settings, the user simply needed to provide the training data for different conditions.

4.6 Conclusions

In this chapter a complete image processing and classification algorithm for yeast cell morphology had been presented. The algorithm contained four sequential processes, first an image enhancement process that removed background noise and improves image quality, then a segmentation algorithm that converted the images to a binary matrix that contain the cell shape, followed by feature extraction methods, and a self-learning k^{th} nearest neighbour (kNN) classifier that distinguished between non-budding, small bud and large bud cells. It was found that the image enhancement algorithm was capable of removing the effect of uneven illumination and sensor noise. The most accurate and efficient feature space for classification between budding and non-budding cells was the axis ratio & compactness feature space, while the compactness & bud ratio feature space was capable of classifying between cells with small and large buds. The class shapes in these feature spaces were not Gaussian due to the number of outliers, and none of the classes were linearly separable; thus the kNN classifier was the most accurate classifier compared to the support vector machine and Mahalanobis distance classifiers.

The algorithm was also tested under different illumination and focus settings and it was found that under low exposure settings the higher noise results in lower accuracy. The system could tolerate a slight variation in focusing, but for under focused images a different segmentation algorithm needed to be implemented for accurate classification. The algorithm also worked for different microscope settings, although different training sets needed to be provided.

Chapter 5. Image Based Flow Cytometry

In chapter 4 it was mentioned that, understanding of cell cycle regulation is an important topic in many fields of biological research. The budding yeast cells, Saccharomyces cerevisiae, are frequently used as a model species to study cell cycles mainly because the yeast cell cycle progression is easily monitored via changes in cell morphology. However, automated techniques for identifying and sorting yeast cells based on their cell cycle phases have not been well studied. Such a system that measures and sorts cells based on their properties are referred to as a flow cytometry system. The goal of this chapter is to develop an intelligent flow cytometry system that can identify cells in different cycle phases using the image processing techniques mentioned in chapter 4, and isolate and collect cells in the desired phase.

5.1 Existing Flow Cytometry Technology

Cytometry is the measurement of cells based on various physicochemical parameters, while flow cytometry is the cytometric analysis of cells suspended in a flowing liquid media. Recent flow cytometry systems often include the ability of to separate and isolate cells based on their parameters[Huh 2005], and flow cytometers are therefore also referred to as cell sorters. A flow cytometer consists of three major components: the focusing element, the detection unit, and the sorting mechanism (Figure 36).

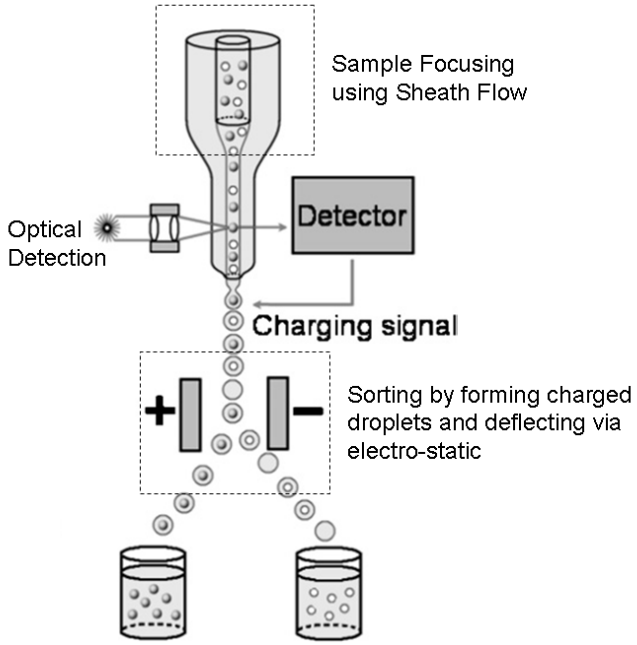

Figure 36 Schematic of a conventional FACS droplet sorter. Droplets containing cells are formed and charged at the nozzle, then deflected by charged plates into collectors [Huh 2005]

Commercial products typically use fluorescent probes that stain cellular components or functions as its detection unit [Shapiro 1995], and are commonly referred to as fluorescence-activated cell sorter (FACS). Becton Dickinson and Company (BD) manufactures the FACSCalibur system, which can detect 6 different parameters based on different fluorescence and scattering at speeds up to 60,000 analyses per second, and sort cells via charged fluid droplets to achieve a cell capture rate of 300 cells per second [BD 2009]. The analytical capabilities of flow cytometry are finding increasing applications in cancer diagnosis [Rieseberg 2001], pharmacology [Andersson 2003], genetic research [Huh 2005], and food and water quality monitoring [Yamaguchi 2003].

Although commercial flow cytometry systems provide rapid and reliable analytical capabilities, they are also typically bulky, expensive, mechanically complex, and require specialized operators and a relatively large volume of the sample [Huh 2005]. These drawbacks have motivated efforts to design micro fabricated microfluidic devices to achieve smaller, simpler, and inexpensive flow cytometers. Over the last fifteen years there have been numerous attempts to miniaturize the flow cytometer, with many different technologies proposed. This section will review the existing techniques used in the three major components of a microflow cytometer, and propose a flow cytometry design for the morphological classification of yeast cells.

5.1.1 Sample Focusing

The purpose of the sample focusing unit is to ensure the samples pass through the detection unit one at a time so they can be analyzed individually, as well as confining the position of the cells to reduce the size of the detection area. The existing focusing methods can be roughly grouped into two different types: the constricting channel, which focuses the samples by forcing them into a narrow channel slightly larger than the cell size (Figure 37a), and the sheath flow, which uses two extra focusing channels to force the particles into the central streamline (Figure 37b).

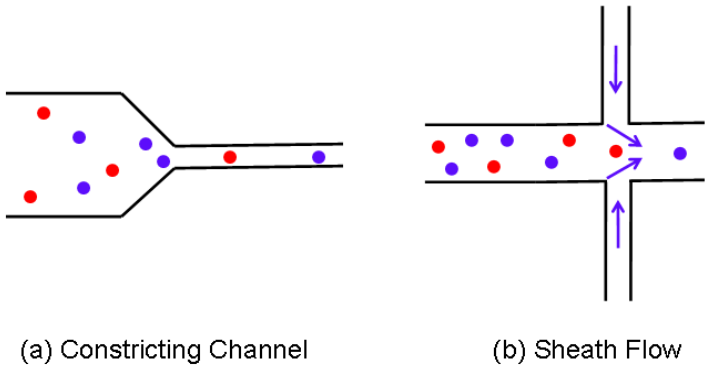

Figure 37 Different Types of Sample Focusing

Constricting channel focusing is easy to fabricate, easy to control, and ensures the sample are always confined. However, it comes with many disadvantages. The narrow channel is prone to clogging and particles contacting/sticking to the channel wall, as well as requiring high pressure due to high resistance, and cannot adapt to different cell sizes. Nonetheless,

constricting channel focusing has been used in some cell sorter designs [Fu 2002; Johann 2004].

The majority of flow cytometers use some variation of sheath flow focusing. Sheath flow focusing allows more control over the speed and spacing of samples, and the designer can also vary the junction geometry to change the focused stream width to adapt to different cell sizes [Taylor 2008]. The disadvantage of sheath flow focusing is the potential for particles to drift away from the central streamline.

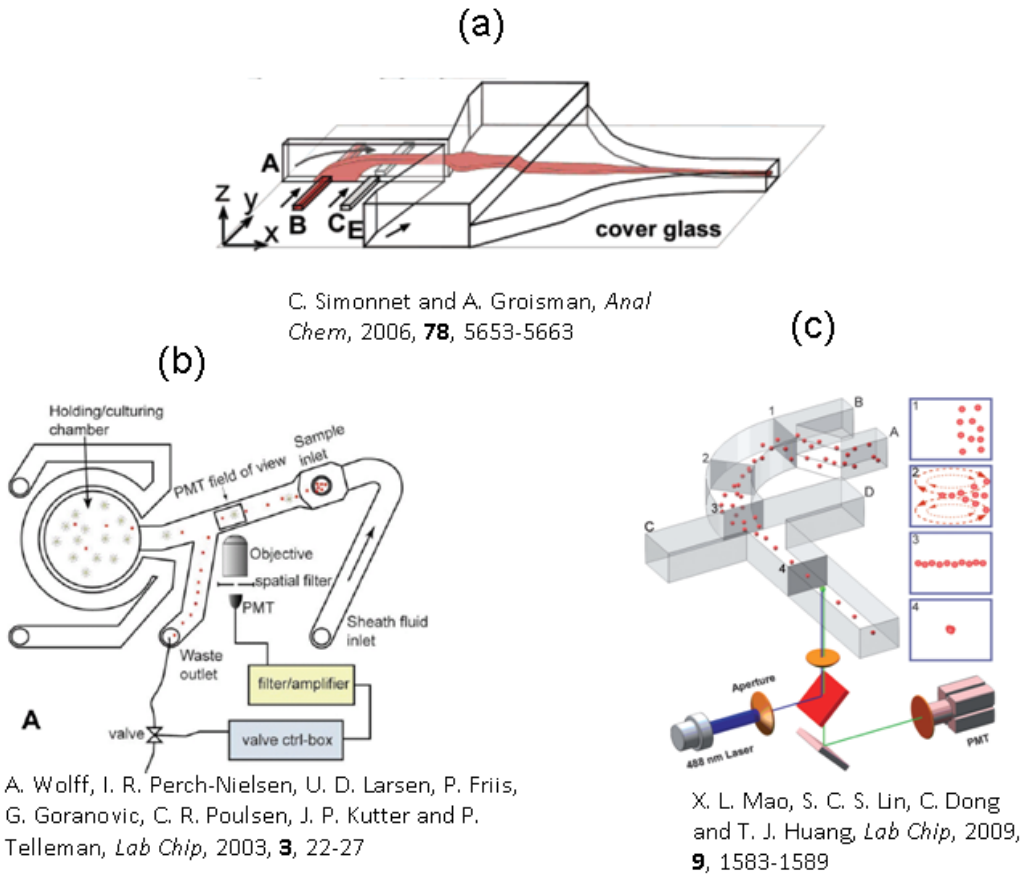

Figure 38 Different 3D Sample Focusing Techniques

Conventional sample focusing units are 2D mechanisms, meaning that is the particles only get focused onto a plane, with their locations confined horizontally, but not vertically. This is not a significant problem if the detection unit is above or below the channels, but miniaturized detection units, such as optical fibre and waveguides, are usually placed in-plane with the fluidic channel, thus 3D focusing mechanism are required to ensure perfect alignment of

samples and detector. Simonnet et al, reported a 3D focusing structure using two shallow channels (Figure 38a), effectively combining the sheath flow and constricting channel focusing together [Simonnet 2006]. Wolff et al, achieved 3D focusing using a chimney structure (Figure 38b). This allows channel depth to be increased to reduce the risk of clogging, and they were able to achieve very high throughput [Wolff 2003]. Mao et al, demonstrated 3D focusing using microfluidic drifting [Mao 2009]. This method only requires a simple planar chip design (Figure 38c), compared to the other two, both of which require complicated multi-level PDMS structures. However, the microfluidic drifting method must be performed with very high flow speed that is difficult to control, and the dimensions are dependent on particle sizes.

5.1.2 Detection

The detection unit is the most important piece of all in flow cytometry. It is the intelligence of the system, as it serves the purposes of detecting the presence of a cell, measuring the cell properties, as well as making sorting decisions. Nearly all the reported microfluidic flow cytometers use optical based detection, which contains a laser source that directs a focused light beam onto the cells, and a series of photo detectors, typically avalanche photodiodes (APD) or photomultiplier tubes (PMT) that captures light scattered at different angles and fluorescence emissions at several wavelengths for each individual cell [Huh 2005]. This set of data can then be analyzed statistically to obtain parameters of the cells.

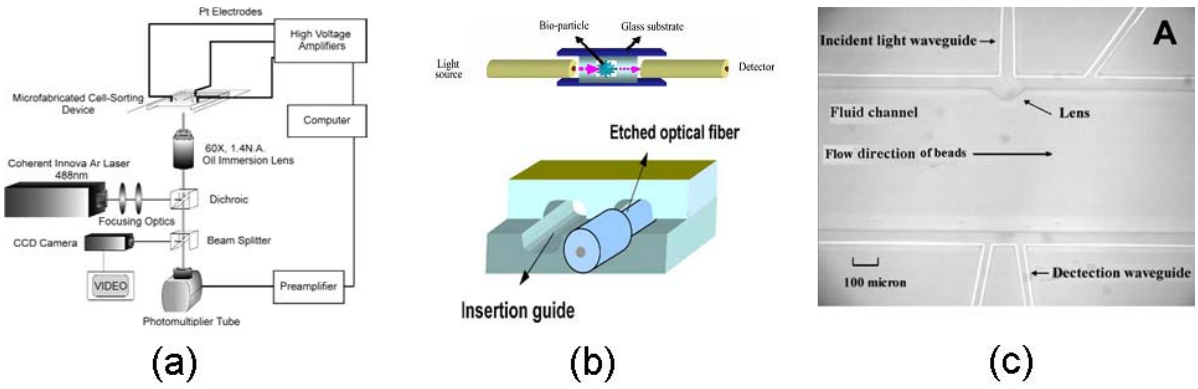

Figure 39 Different Optical Detection Setups

Commercially available optics can be used externally for detection in microflow cytometers [Fu 1999; Kang 2008]. They are widely available, allow easy setup and do not complicate the microfluidic chip design, however, external optics (Figure 39a) are typically bulky, difficult to

multiplex, and can cost up to $15,000 for a simple setup. Thus, the current trend in optical detection is toward using integrated optical elements, typically on-chip waveguides, to design miniaturized devices. One way to fabricate an on-chip waveguide is to insert optical fibres into the chip and through designated channels as guides, shown in Figure 39b [Fu 2004]. However, the insertion process is difficult with low-repeatability, making this technique un-suitable to systems incorporating multiple excitation sources, filters, or detectors [Ateya 2008]. An alternative method is to directly build an on-chip wave-guide with polymers. For example, Godin et al, created an all-PDMS device with integrated PDMS waveguides by varying the fabrication parameters of PDMS [Godin 2006]; Wang et al, built a flow cytometer with integrated waveguides and lenses (Figure 39c) using the photoresist SU-8 [Wang 2004]. However, waveguides fabricated in this manner tend to make the final chip bonding process difficult, and the roughness of the waveguide usually results in high attenuation [Ateya 2008]. Other problems common to optical detection methods include low signal-to-noise ratio, and alignment difficulties of samples and detectors.

Recently, several attempts have been made toward detection using microscopic imaging [Lee 2005; Kovac 2007; Lin 2008]. The image based detection method for flow cytometry is not widely used mainly due to the speed limitation, both shutter and acquisition speed, of CCD cameras, as well as the difficulty of building a miniaturized device with integrated lens and sensors. However, microscopic imaging detection has many advantages unique to itself: 1) the external equipment required (microscope and camera with computer interface) are the standard equipment in most laboratories, thus no additional equipment needs to be purchased; 2) advancements in image processing algorithms can be utilized to eliminate noise, enhance signal quality, and obtain morphological or sub-cellular information accurately and intuitively; 3) the detection algorithm is completely software based, which can be modified easily for different cells/particles without redesigning the mechanical components, and 4) there will be no on-chip integration of optics, thus eliminating complicated fabrication and alignment issues. Because of these advantages, for laboratory use with low-throughput requirements, such as academic research, microscopic imaging detection is a much more cost-effective, accurate, adaptive, and user-friendly method over traditional optical detection techniques. Therefore, it has been chosen as the detection method in this research.

5.1.3 Sorting Mechanism

The sorting mechanism of a cell sorter must be capable of directing individual cells into different collection reservoirs. There are a variety of techniques that can be used to physically manipulate a specific cell, and they achieve this by either changing the flow field inside the fluidic channels, or directly applying a force to the cell to move it across streamlines.

Electroosmotic flow (EOF) switching is a widely used method for sorting. A typical EOF cell sorter usually uses EOF as the driving force for fluidic flow in the chip, and achieves switching of fluid streams by changing the electrical potentials at the outlets, which in turn changes the flow field and direct cells into different paths [Fu 1999; Taylor 2008]. The advantages of EOF flow are that the velocity profile is essentially plug-like and allows easier prediction of particle velocities, and changing electrical potential results in immediate change in flow direction [Taylor 2008]. However, the number of drawbacks to EOF is also abundant. First, non-charged particles can acquire charges on them in the EOF, which result in hard-to-predict particle motions. Secondly, a large electrical field is usually required, which can be dangerous for bioparticles. Thirdly, expensive equipment is needed to generate high electric potentials. Other problems also include the compatibility requirement of buffer solutions, and its dependency on channel surface properties, to name a few.

Dielectrophoresis (DEP) is a phenomenon in which a force is exerted on a dielectric particle when it is subjected to a non-uniform electric field, differences in dielectric properties of cells and particles allow their handling by the DEP force. By building on-chip electrodes, the DEP force can be used as a trap to capture cells [Voldman 2002], as a switch to selectively manipulate cells[Lee 2005; Tai 2007; Lin 2008] and droplets [Baret 2009], or to directly separate particles based on their dielectric properties [Choi 2005]. The particle handling ability of the DEP force can also be used for sample focusing. Lin et al, used the DEP force along with sheath flow to achieve 3D focusing of particles [Lin 2004].

The popularity of DEP is attributed to its advantages of low voltage requirement and the small, non-harmful force it applies directly to the particles. However, the electrode design for DEP is usually extremely complicated, and thus hinders its application [Lin 2008].

Both the EOF and DEP methods described above use electrical energy to manipulate particles in the cell sorter. It is also possible to building a cell sorting mechanism using only mechanical valves to control the flow into different outlets. Early generation of micro valves were slow, prone to leakage and dead volume, as well as having a large footprint with a complicated fabrication process. However, this has been changed with the introduction of monolithic microvalves created using the technique of multilayer soft lithography [Fu 2002] . The new type of microvalve consists of a pneumatically actuated membrane that opens/closes a microfluidic channel, which has millisecond reaction time, no leakage or dead volume, and is simple to fabricate [Unger 2000]. The monolithic microvalves have already been used in a variety of microfluidic applications including flow cytometry. Ohnuki et al, reported a microfluidic device that uses the membrane structure of the microvalve to trap yeast cells for high-magnification microscopic imaging [Ohnuki 2009]. Fu et al, created a cell sorter with integrated micropumps using this technology, and were able to successfully sort live E. coli cells [Fu 2002]. Fu's work demonstrated that the monolithic valves can be used to make fully integrated cell sorters with pumping, flow switching, and the potential for the addition of many different operations; the valves are also gentle enough to handle bioparticles. This type of monolithic microvalve is chosen in this study to build a sorting mechanism, although it does have the disadvantage of requiring a bulky external control system.

5.1.4 Project Scope

As mentioned earlier, the goal of this project is to design a device for yeast cell cycle study. The major functionality of this device is being able to identify yeast cells in different cell cycle phase and isolate cells in the desired phase, while having the ability to immediately treat cells either before or after sorting with minimal time variation and sample loss. To this end, a cell sorter with microscopic imaging detection and integrated monolithic valves and pumps is proposed. The monolithic valves and pumps allow precise control of liquid flow, the image processing detection is capable of cell cycle phase classification based on yeast cell morphology (refer to chapter 4), and the integrated micro fabrication method can be used for inclusion of other functionalities. The sample focusing element will use sheath flow rather than a constricted channel for its adaptability. 3D focusing is not required since the yeast cells are relatively large (~ 5μm diameter), and the optical properties of the cells allow good imaging quality even when cells are slightly out of focus (refer to chapter 4).

5.2 Design Overview

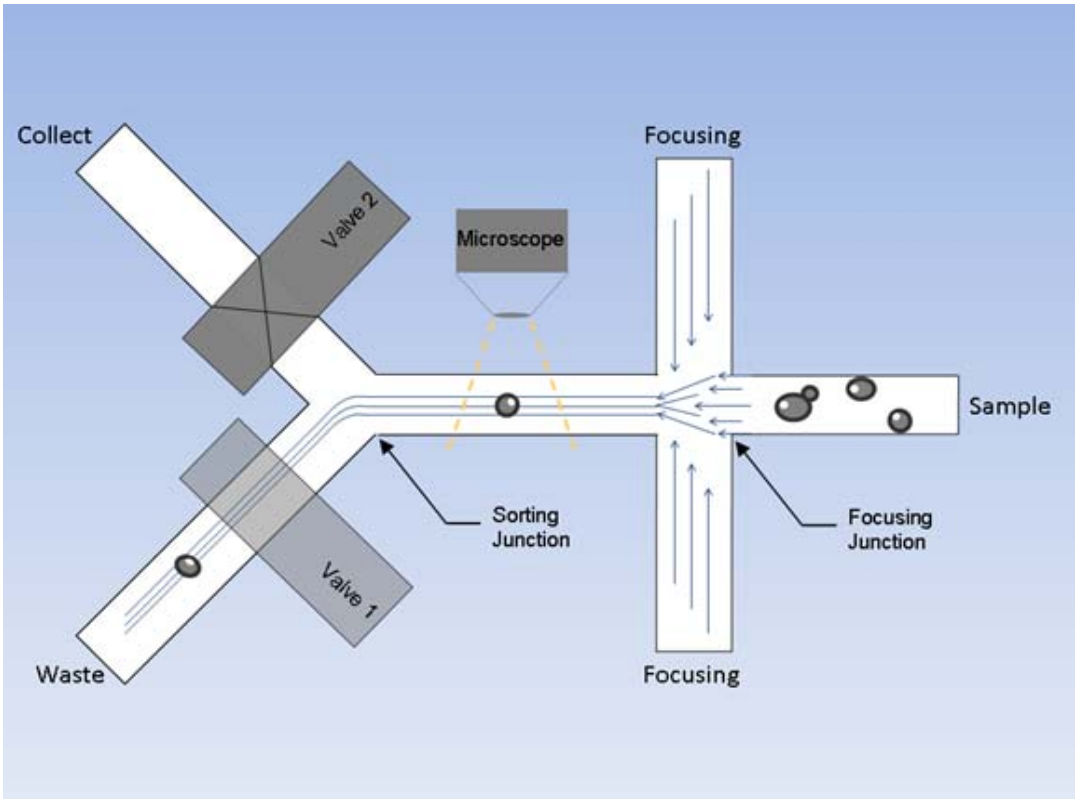

Figure 40 Schematics of the Cell Sorter

Figure 40 shows the operating principle of the cell sorter to be made. The samples come in through the sample reservoir and pass through a flow focusing unit, which uses sheath flow to pinch the sample stream and aligns the samples into a single file. Then the cells pass through the observation channel, which is monitored by the Nikon eclipse Ti microscope. An intelligence decision making algorithm processes the image looking for a cell. If a cell is found, the system classifies it as either budding or non-budding, and then opens/closes the two valves in the two sorting channels to direct the destination of the cell into either the collect reservoir (budding cells) or the waste reservoir (all others). The flow focusing unit and the sorting mechanism are the mechanical component and the external electronics that control the pumps/valves are part of the electrical component of this system, while the imaging and decision making algorithms are the intelligence component. Each of these components is further explained below.

5.2.1 Electro-Mechanical System

The electro-mechanical component of the cell sorting system consists of the microfluidic chip with integrated valves, and the external microvalve controller. The microchip has two layers of channels. The top layer has the fluidic channels that are consisted of a crossing-linked channel structure for sheath flow sample focusing, followed by a Y shape junction for sorting (shown in Figure 41). The bottom layer has the control channels that control the integrated pumps and valves. The fluidic channels have a width of 60µm and a channel height of 20µm. The control channels all have widths of 100µm, thus all valves have an active area of 60 x 100µm. The peristaltic pumps are made of three valves in a row, with a distance of 100µm between each valve. The control channels have a height of 40µm and the membrane thickness is roughly 15µm (1600rpm PDMS spin coating).

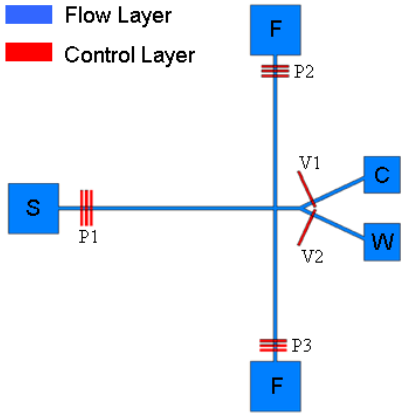

Figure 41 Cell Sorter Design Schematics.

The sample channel and the two focusing channels all have the same length of 7.5mm, this is to ensure the pulses of the three peristaltic pumps arrive at the focusing junction at the same time to reduce mixing and backflow. The channel between the focusing junction and the sorting junction has a length of 1mm, and the collect/waste channels have lengths of 3mm. beside the above mentioned sorting chip (design #1), two alternative designs are made: one design with serpentine collect/waste channels to increase the length of these two channels from 3mm to 20mm, for storing and potentially retrieving of sorted cells (design #2); and one design with the fluidic channel height of 10µm instead of 20µm. Since yeast cells have an average diameter of 5µm, a channel height of 10µm should confine the cells more to the center of the channel than 20µm, and result in better imaging quality.

Each individual microvalve needs to be controlled using an external pneumatic valve. A control system that contains all the necessary pneumatic and electronic components are made and described in chapter 3. The controller can control up to 32 valves, and communicate with a PC via serial port. For peristaltic pumping, the three valves must be actuated by the pattern of 110, 011, 001, 101, where 0 and 1 indicate “valve open” and “valve close”, respectively. The time between the actuation of each pattern is called the pumping period, which can be varied between 10ms to 500ms. A delay can also be introduced between each pattern cycle to alter the pumping speed (cycle delay): 1 cycle delay between each pattern cycle is equivalent to half of the original speed, 3 cycles delay between each pattern cycle is quarter speed, and 7 cycles delay between each pattern cycle is one-eighth speed.

5.2.2 Intelligence System

The intelligence system includes three components: sensing, decision making, and actuation. A flow chart that shows the interaction of these components is shown in Figure 42.

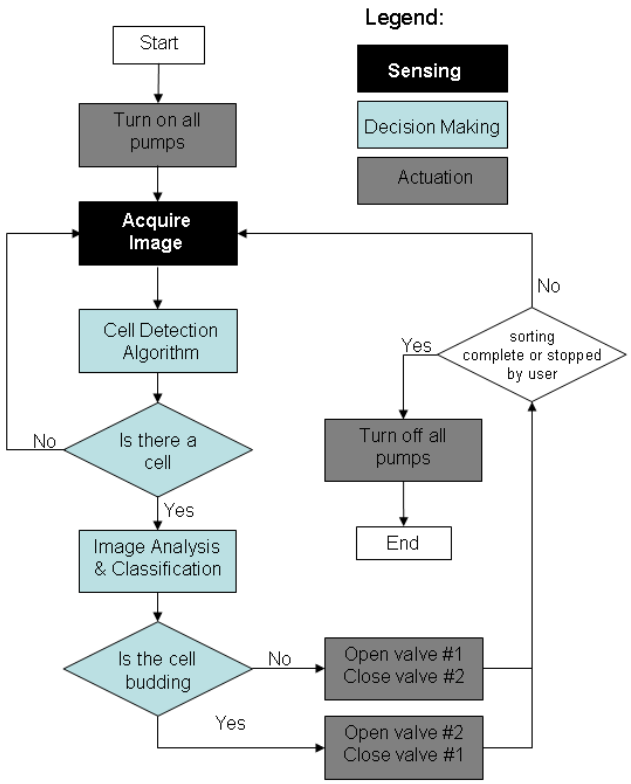

Figure 42 Flow Chart of the Intelligence Algorithm

Sensing was done through the use of the QImage CCD camera mounted on the Nikon eclipse Ti microscope. The magnification on the Nikon microscope was 30X (20X objective with a 1.5X internal multiplier), with a field of view of roughly 900x650μm. A view of the micro channel near the focusing junction was shown in Figure 43. The QImage camera allowed the user to define a region of interest (ROI) so that only the part of the image that contains the channel was acquired, which reduced the acquisition time. The signals for actuation were encoded-8-bit command words, sent via a serial port that connects the PC to the valve controller. For details of the optical and hardware setup please refer to chapter 2 and chapter 3.

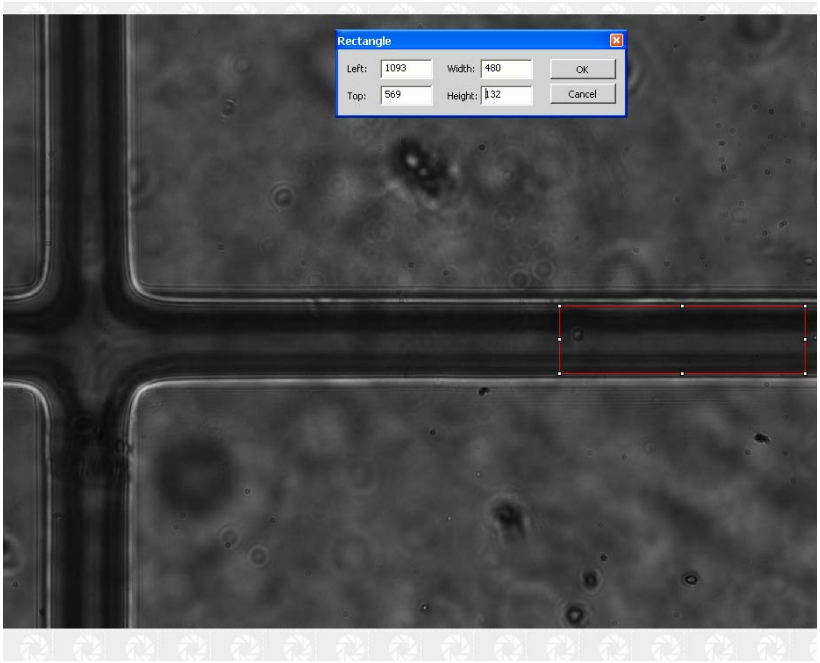

Figure 43 Nikon Microscope Field of View

The intelligence system was implemented in Matlab. The program, once started, runs for a pre-defined number (usually 500) loops. At the start of each loop, the program would call the QImage camera to capture an image of the channel (Acquire Image block); this image was then scanned from the upstream side toward the downstream side for the presence of a yeast cell (Cell Detection Algorithm block), If a cell was not found, the image was discarded and an a new image was captured. If a cell was found, then a 60x60 pixel region surrounding the cell would be saved and passed into the image analysis & classification algorithm; this algorithm would process the image, extract geometrical features from the cell, and classify it based on pre-defined training data provided by the user as having no bud (G1 phase), a small bud (S

phase), or a large bud (G2 and M phases) (details of this algorithm were described in chapter 4). If the cell had a small bud (in the S phase), the valves would be switched and the cell propelled into the collect channel (Figure 41); if the cell was not in the S phase, it would be propelled into the bottom channel. After the cell passes through, the valves would not switch until next cell came through the ROI, and the valves only switch if the next cell was classified differently. While the program is running, all three pumps would be on, and when the program is finished the pumps would stop and seal the channels to prevent fluid flow due to induced pressure differences. Different speed settings of the pumps would result in different sorting speed and accuracy, and needs to be evaluated.

Intelligence System Speed

By estimating the average computational time required to complete one loop of the intelligence program, the frame rate of the system could be calculated. The first delay in the loop came from the image acquisition. The QImage CCD camera connected to the Nikon microscope could take full resolution (1600x1200 pixel) images at a frame rate of 5 fps, or it could operate at its maximum frame rate of 30 fps and took images of resolution 640x480 pixel or less. The maximum frame rate must be maintained to reduce the effect of discretization and ensure adequate sorting speed. High resolution could be maintained by defining a smaller region of interest (ROI), shown in Figure 43. Thus the time delay due to image acquisition was constant and can be a minimum of 33ms.

The time delay due to the cell detection algorithm was not constant. This algorithm worked on the principle of scanning the pixels of the region of interest (ROI) in a predefined order, thus image frames with no cells in them would take the longest time, while frames with cells would take less time to scan. Moreover, the size of the ROI also significantly affected the computation time. To reduce computational time, only one in five rows was scanned, and for each row, only one in five pixels was scanned. The computational delay of the detection algorithm was obtained using simulation described later in this section.

The feature extraction and classification processes together had a constant delay, since they operate on a constant size (60x60 pixels) image clip. The classification process used a kNN

classifier with 100 pre-defined training data. The two processes combined for a delay of 35ms. However, this delay would not occur every time in the program loop, but would only occur when a cell was present. A cell also could not be in every single frame, otherwise the concentration of the cell would be too high for the sorting mechanism to function accurately. A good concentration of cells had one cell in every ten frames (details would be discussed in the next section), thus the average time delay due to feature extraction and classification was ~3.5ms per loop. Combining these three sources of delay gave the total loop delay. The frame rate of the system (the number of frames it can scan every minute) is equal to the reciprocal of the total delay. The frame rate for different ROI sizes were tabulated in Table 8

Simulations were done to estimate the frame rates for different ROI sizes. The simulation applied the cell detection algorithm to a user generated image with no cells in it, and used the Matlab timer function to obtain the time required to process this image. Five different ROI sizes were simulated: all have the same width of 170 pixels, since the micro channel width was constant, and all were less than 640x480 pixels to ensure the maximum camera frame rate. The "Total Loop Delay" is obtained by adding 37ms to the scan time to simulate the effect of image acquisition and feature extraction/classification.

Table 8 Simulated Computational Delays for Different ROI Size

Region of Interest [pixels (μm)]		Max Scan Time	Total Loop Delay	Average Frame Rate
1200x170	(440x60)	50ms	87ms	11.5
1000x170	(366x60)	42ms	79ms	12.6
600x170	(220x60)	26ms	63ms	15.8
340x170	(124x60)	15ms	52ms	19.2
170x170	(62x60)	8ms	45ms	22.2

The simulations showed that larger ROI sizes yield lower reduction in frame rate, as long as the maximum camera frame rate criterion is maintained. However, this effect could result in redundant information, such as one cell staying in the ROI for many frames, and breaks the assumption of 1 cell in every 10 frames. Thus the ROI should be made smaller as long as it does not miss any cells.

5.3 Experimental Design Validations

This section detailed the experimental processes used to validate design parameters of the cell sorter chip.

5.3.1 Micro Fabrication

The chip was fabricated using multi-layer soft lithography techniques. The control and fluidic layers were cast from two different molds fabricated on silicon wafers. Both molds were made using photolithography, with the fluidic layer mold made of AZ50XT photoresist, while the control layer made of SU-8 photoresist. The microchip itself was cast using PDMS elastomer (Sylgard 184). About 3~4mm thick PDMS was poured onto the fluidic layer mold, while PDMS was spin coated onto the control layer mold to a thickness of 60μm. The two castings were cured on hotplates slightly until the elastomer just harden, the fluidic layer cast was then peeled off and bonded to the control layer and baked until the elastomer had cured completely, forming an irreversible bond between them. The PDMS casting was then removed from the mold, and cut into a 40mm x 25mm square piece. Access holes to the reservoirs were punched and the piece was bonded to a glass slide to form the microchip (Figure 44).

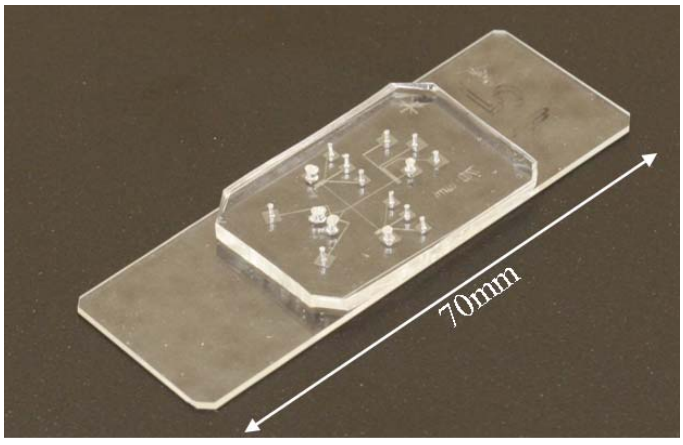

Figure 44 Final Product of the Flow Cytometry Microchip

During the fabrication of the different chip designs, it was discovered that the design with 10μm tall flow channels (design #3) were very difficult to fabricate. The low channel height made the channels collapse easily, thus design #3 was discarded, and only designs #1 and #2, both with 20μm high channels, were fabricated.

5.3.2 Flow focusing

The performance of the flow focusing unit was experimentally tested for both designs (design #1 and #2) under a variety of pumping speeds. Desirable focusing performances should have a narrow focused stream width and minimal mixing between the sample fluid and the focusing fluid. Fluorescent dye was used for the visualization of the focusing.

The following procedure was used for this experiment. The control channels for the pumps were first filled with water, then attached to the solenoid valves for pneumatic control. For the fluidic channels, all reservoirs were filled with 0.5μm filtered DI water and pressurized until all the air bubbles were removed from the fluidic channel network, then fluorescent dye solution was added to the sample reservoir and the pumps for both the sample and focusing channels were turned on. The pumps were allowed to run until the fluorescent dye solution was completely propelled into the sample channel. The Olympus BX51 microscope (10x objective) with COOLSnap camera was then used to record the focusing action at the focusing junction. The pumping period was varied between 50ms and 500ms, and cycle delays were added to either the sample channel pump or the focusing channel pump to produce uneven pumping speed from them. The images showing the focusing action for different conditions were shown in Figure 45.

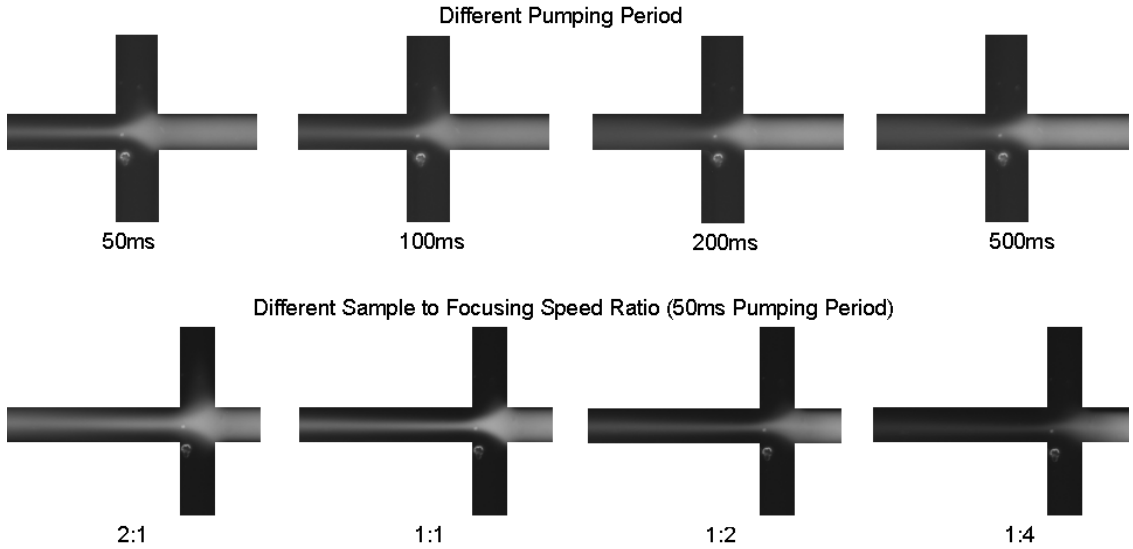

Figure 45 Flow focusing for different pumping period and different sample to focusing speed ratio. (Design #1, all images taken with 2 second exposure)

The results from different pumping periods showed that smaller pumping period (higher pumping frequency) yielded a more confined focused stream with less diffusion across the streamlines. This was expected since with high pumping frequency the damping effect of the PDMS channel was more relevant, and thus the fluid velocity was smoother. With lower pumping frequency the pulsing effect from the peristaltic pump was stronger, resulting in stronger diffusion.

Different flow speeds in the sample and focusing channels were created by adding cycle delays to the pumps driving the corresponding channel. For example, a sample to focusing speed ratio of 2:1 meant the sample channel pump was operated with no delay, while the focusing pumps had one cycle delay between each pattern cycle. Changing this ratio effectively changed the focusing stream width. Having higher sample speed (ratio 2:1) than focusing speed did not create thin and confined focused stream as desired, while experimental observations show that very low sample speed (ratio 1:4) resulted in unstable flow at the focusing junction: any disturbance could result in focusing fluid flowing back into the sample channel. In the result for the 1:2 speed ratio, the focused stream had the same width as the 1:1 ratio, but the brightness of the fluorescence was dimmer because of lower concentration due to diffusion. Thus the 1:1 ratio was the best option. The focused stream width could be estimated by measuring the width of the bright stream in the images, and the stream width of the 1:1 ratio was estimated to be 15μm. Since the yeast cells had an average diameter of 5μm, this focused stream width was adequate for focusing yeast cells.

Figure 46 Flow focusing – Design #2. (50ms pumping period, 2 second exposure)

Figure 46 showed the experimental flow focusing result with design #2 – longer collect/waste channels. Compared to design #1, which had very short outlet channels, this design had very narrow focused stream (barely visible in Figure 46), and observations suggest it also had

unstable flow at the focusing junction (lack of symmetry shown in Figure 46). This is due to the high downstream resistance, which created a high pressure point at the focusing junction that could drive the fluid back through the peristaltic pump.

The flow focusing experiments showed that focusing with the micro fabricated peristaltic pump was difficult due to active mixing and unstable flow field, but it was possible to achieve good performance under certain operating conditions. The downstream resistance of the focusing junction must be significantly smaller than the upstream resistance to prevent backflow (design #1 has a ratio of 1:3 downstream to upstream resistances), and the pumps for all sample/focusing channels must operate at the same frequency and be synchronized to reduce active mixing. High pumping frequency would also be recommended.

5.3.3 Sorting simulation using fluorescent beads

Before live yeast cells could be being tested in the chip, the sorting system was tested by using fluorescent particles. The goal of this simulation was to determine the reliability and limitation of the sorting mechanism. Since the image analysis could not be applied to fluorescent particles, this simulation would only try to identify the particles passing through the region of interest (ROI), then separated them based on their order of passing. For example, the 1^{st}, 3^{rd}, 5^{th}… particles to pass through the ROI would be directed to one reservoir, while the 2^{nd}, 4^{th}, 6^{th}… particles to go through would be directed to the other reservoir. The sorting program would need to be modified slightly. In the detection algorithm, the criterion for detecting a particle was now a threshold on the maximum pixel intensity in the ROI. The cell isolation, feature extraction, and cell classification algorithms could be omitted. Since the particle detection algorithm was different from the cell detection algorithm, the frame rate of the simulation was similar to but did not match the frame rates of the actual system. The Olympus BX51 microscope was used for the visualization of fluorescent particles, while other portions of the system remained the same.

Chip design #1 was used for this simulation with a pumping frequency of 20Hz (period 50ms) and maintaining the same speed for all pumps. The chip was filled with 1% PEG Diacrylate aqueous solution, and pressures were applied to the inlets to remove any air bubble trapped in the channels/reservoirs. The fluorescent particle solution (cf. chapter 2) was diluted to 0.1%,

(about 2 x 10^7 particles/ml), and 1% PEG Diacrylate was added. 10ul of the fluorescent particle solution was added into the sample reservoir using a pipette, and the modified sorting program was started with the ROI set to approximately 500μm upstream of the sorting junction. For evaluation purposes, the maximum pixel intensity in the ROI at each frame was saved, and the sorting process was recorded as a movie through the eye-piece using a point-and-shoot digital camera.

Since the Olympus BX51 microscope was used instead of the Nikon eclipse Ti, the microscope objective, camera, and field of view are all different: one pixel in the Olympus' field of view was roughly two pixels in the Nikon's. Experiments were conducted for three different ROI sizes: 350x100, 200x100 and 100x100 pixels, which correspond to 600x170, 340x170 and 170x170 pixels on the Nikon eclipse Ti. 1500 frames for each ROI were recorded with average frame rates of 15.3, 16.4 and 17.4fps respectively. Then the recorded sorting movie was compared with the plot of maximum intensity during the sorting process; an example of such a plot was shown in Figure 47 below.

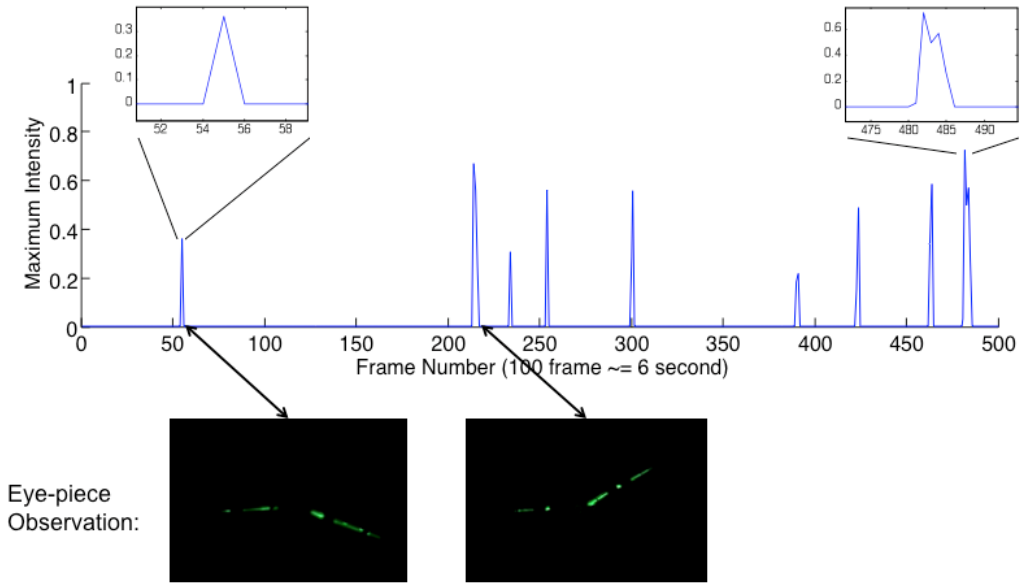

Figure 47 Sample plot of maximum intensity during sorting. The eye-piece observations show the path of a single fluorescence particle by superimposing multiple frames. (a full movie of the sorting process available)

Each peak in the above figure corresponded to a fluorescent particle detected by the system, and the number of peaks should equal to the number of particles observed through the eye-piece. The width of each peak represented the duration that a particle is visible in the region of interest, for example the first peak had a width of 1 frame, while the ninth peak had a width of 5 frames. By comparing the miss-sorting in eye-piece observation and the peak plots, one could also determine the minimum distance between particles required for the sorting mechanism.

Table 9 below showed the tabulated results of the simulation. The minimum speed was estimated by taking the length of the ROI, dividing by the maximum peak width observed, and multiplying by the frame rate. The results showed that, for a region of interest equal to or smaller than 200x100, the program could not guarantee that all the particles passing through it were identified. This was expected since a smaller ROI meant a higher chance of a particle passing through it between frames. The result also confirmed that for the sorting mechanism to work properly, the particles must be properly spaced apart, and based on the observations, 10 frames should be the minimum spacing to ensure proper sorting.

Table 9 Result of Fluorescent Particle Sorting Simulation

Region of Investigation	Frame rate (fps)	Particles identified by program (%)	Minimum speed observed (μm/s)	Minimum spacing between particles properly sorted (frames)
350x100	15.3	100%	680	6
200x100	16.4	90%	520	5
100x100	17.4	74%	560	4

With the minimum spacing between particles determined, and the minimum speed and channel dimensions available, a limit on the cell concentration could be calculated. First estimate the flow rate (q) by assuming minimum particle speed equal to average fluid speed:

$$q = V_{\min} \cdot A = V_{\min}(2/3) \cdot w \cdot h = 0.548\, nL/s$$

where w and h are the channel width and height respectively. Next convert the flow rate from volume per second to volume per frame, then multiply by ten to get the volume flow rate per 10 frames:

$$V_{10f} = 10 \cdot V_{\min} / fps = 3.59\, nL/s$$

where *fps* is the frame rate per second of the system. According to the required minimum spacing, there should be only 1 cell in the volume of fluid per 10 frames, to increase the tolerance, assume there is 0.5 cell in the volume of fluid per 10 frames. Now compute the maximum cell concentration (*Conc*) to ensure proper sorting:

$$Conc = 0.5/V_{10f} \approx 2\times10^{6}\ cells/mL$$

However, this concentration is the cell concentration after being diluted by the sheath flow focusing, thus the cell solution at the sample inlet should be 3 times more concentrated. Therefore, a safe cell concentration to ensure accurate sorting would be between 0.5~1x10^7 cells/ml

5.4 On Chip Cell Counting

The experiments had validated all the necessary design components of the flow cytometry system, and the design parameters are recapped as:

Chip design	**Image system**	**Material**
Fluidic channel dimensions: 60μm wide by 20μm high, sample/focusing channels length: 7.5mm focusing junction to sorting junction distance: 1mm collect/waste channel length: 3mm Control channel dimensions: 100μm wide by 40μm high membrane thickness: 15μm Valve/pump operation: pressure required: 160kPa pumping period: 50ms (20Hz) all pumps maintain same speed	Nikon eclipse Ti microscope, 20x objective with 1.5x internal multiplier. Region of interest (ROI): 600x170pixel, or 220x60μm	add 1% PEG Diacrylate in the cell culture media as surfactant; Use cell solution with a concentration between 0.5~1x10^7 cells/mL

An experiment was performed in the flow cytometry system to identify and isolate yeast cells in the S phase from the rest of cells. However, the current chip design and optical setup did not allow the user to retrieve the cells after sorting, and had no ability for validating the sorting accuracy. The Nikon microscope did not support eye-piece observation while the camera is in use. The short collect/waste channel could not store cells for inspection, and cells in the

reservoir could not be observed clearly because of the outlet hole in the PDMS (in chapter 6, recommendations would be made to complete the cell retrieving portion of the system). Therefore, the flow cytometry system was effectively only a cell counting device, and thus the goal of this experiment was to count the number of cells passing through the sorting channel and how many of them were in the S phase.

To prepare for the experiment, the control channels of the chip were filled with water and then connected to the pneumatic solenoid valves. The fluid channels were filled with cell culture media with 1% PEG Diacrylate, to ensure a safe and familiar environment for the cells to reduce the effect of a rapidly changing environment. Meanwhile, the cell solution with concentration $1x10^7$ cells/mL was prepared, and kept agitated with a magnetic stirrer. The intelligence software was initialized to run for 1000 loops, the region of interest set to an area approximate 500μm upstream from the sorting junction, and the program slightly modified to save all the frames that contain cells, and the class that was assigned by the classifier. A pipette is used to deliver 10μl of cell solution into the sample reservoir, and then sorting is started.

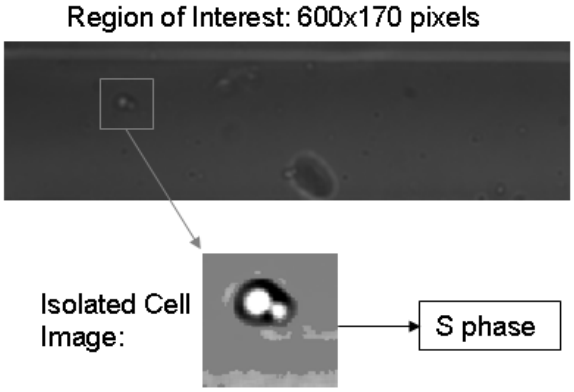

Figure 48 Example of Image Frame Containing a Cell

In total 96 cells were found from the 1000 frames; an example of the recorded image frame is shown in Figure 48. The system result was compared with the actual cell class, which was determined by inspecting the saved image frames, in Table 10

Table 10 Performance of Flow Cytometry System with Live Yeast Cells

		Classifier Results		
		1	**2**	**3**
Actual Class	**1**	58	2	0
	2	1	13	0
	3	2	0	20

The cell counting experiment showed very promising results, with very few misclassifications of cells. There was approximate 1 cell in every 10 frames, which matched the previous calculated value. The experiment found that about 15% of yeast cells were in the S phase, this value only deviated slightly from the study conducted by Hartwell, which suggested that S phase yeast cells make up 25% of all cell populations [Hartwell 1974]. This deviation is likely caused by the non-ideal cell culture environment and miss-classification of PDMS debris as cells.

The average frame rate during the cytometry process was 15 frames per second, this frame rate resulted in a cell detection rate of approximately 1.4 cells per second. This detection rate was based on real-time analysis.

5.5 Conclusions

This chapter presented the design of a microflow cytometer, for the purpose of developing an automated research tool for classification and isolation of yeast cells in different cell cycle phases. A review of existing flow cytometry technologies was conducted to justify the technologies of choice. The intelligence algorithm was highlighted, and the mechanical components, including sample focusing unit and the sorting mechanism, were thoroughly designed and validated through experiments. Due to limitation of technology, only a cell counting experiment was conducted to show the performance of the system. It was determined this system can accurately classify cells in the microfluidic environment, and can achieve a cell detection rate of 1.4 cells per second.

Chapter 6. Future Extensions

The previous five chapters illustrated the two goals achieved during this thesis project: to bring a complete mLSI system to UW Microfluidic Lab, and to design an intelligent microfluidic system using mLSI technology. However, there is still much room for improvement in both of these goals. Due to time limitations, I will only outline some of the work that can be done in the near future that extend from these two projects.

6.1 Summary of Accomplishments

This thesis project has two major components: 1) the establishment of a microfluidic large scale integration (mLSI) system in the UW Microfluidic Laboratory, and 2) the design of a microflow cytometer for yeast cell cycle identification. Below is a list of accomplishments:

mLSI

1. The protocols for designing and manufacturing of the PDMS microchip with integrated microvalves were developed, including the fabrication of semi-circular channels using AZ-50XT photoresist, and the making of multi-layer PDMS chips using multi-layer soft-lithography.
2. A control system is made, with 32 removable solenoid valves that can control up to 32 microvalves or 8 micropumps on chip, and serial interface to the PC with highly abstracted commands.
3. Valve closing pressures were measured for different valve dimensions, and observations of pumping performances were made for different operating conditions, to recommend some guidelines to designing mLSI systems.

Microflow Cytometry

1. An image processing algorithm that analyzes individual cell clips and performs classification of cell cycle phases was first developed with stationary cell images.
2. A flow cytometer was designed with sheath flow focusing, microscopic imaging detection, and integrated microvalves for flow switching. The various mechanical components were experimentally optimized.
3. Detection and sorting of fluorescent beads were performed with the above mentioned cytometer to verify the system performance – the sorting mechanism functions properly.
4. Performed sorting of yeast cells based on the presence of buds (S phase), at a rate of ~1.5 cells/sec. The detection and classification achieved great accuracy; the sorting could not be verified due to equipment limitations.

The fundamentals for setting up an mLSI system and designing of the cytometer are roughly completed, however, there are still many margins for improvement in both sub-projects.

6.2 Improvement of Microvalves and Pumps

The monolithic microvalve still needs significant improvement in two aspects. First is the actuation method. Currently, each individual microvalve needs to be controlled by its own external solenoid valve. This limitation significantly hindered the mobility of mLSI systems, and limits the practical use of such systems to laboratory only. Efforts have been made to change the current structure of the microvalve. Dr Stephen Quake's group had been leading the revolution, and they have developed a novel microvalve structure that effectively miniaturized the solenoid valve onto the same chip as the monolithic microvalves. However, this new structure would require the fabrication of 4-layer PDMS chips, which would be very difficult.

The second aspect requiring improvement is the design guidelines for the mLSI system. Due to the limited understanding of the fundamental physical properties on the system level, most mLSI systems were designed using experimental validation methods that were mostly trial-and-error. It would be beneficial if numerical analysis tools could be developed for the design of mLSI systems. However, it would be difficult to conduct systematic studies of the microvalve due to unreliable fabrication techniques and inaccurate sensors. The varying elasticity of PDMS would also be a concern. However, the emergence of nanotechnologies will facilitate the development of more accurate fabrication technologies, more sensitive micro/nano sensors, as well as new synthetic materials with more stable mechanical properties in the future. Therefore, future studies at the UW Microfluidic Laboratory should focus on the development of more systematic design guidelines for mLSI systems, by studying the mechanics and dynamics related to the microvalves and peristaltic pumps.

However, future studies should also focus on the application of mLSI to the field of analytical chemistry and biology. The fluid control ability and the margin for integration allow very complicated lab-on-a-chip systems to be designed using mLSI technology. Illustrated below is a proposed biology study that uses the flow cytometer designed earlier.

6.3 Biology study: presents of protein in budding yeast cells

An immediate application of the microflow cytometer is for the investigations on identifying and characterizing protein factors that control the initiation of cell division. The beginning of

cell division (S phase) is believed to be initialized by the presence of certain proteins. These proteins are present at the beginning of S phase to trigger the DNA replication process, and then disassemble toward the end of S phase to prevent re-replication. The current method to investigate the association between certain protein and the cell division process is to genetically modify the yeast cell to link the protein of interest with a fluorescence gene, thus when the protein is present in the cell, a fluorescent spot is also observable in the cell. The researchers would then classify the yeast cells by their cell cycle phase, and try to associate whether the fluorescence is only present in the S phase cells.

The process of classifying yeast cells by cell cycle phase and identification of fluorescence could be performed by the microflow cytometer without much modification. A new chip design was proposed, show in Figure 49, which is similar to the one shown in chapter 5, with large chambers in the exit channels, pumps at the collect and waste reservoirs, and an additional waste reservoir in the reverse direction.

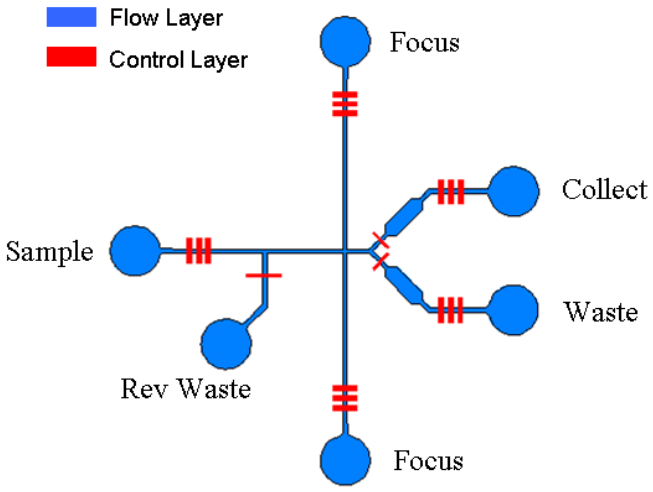

Figure 49 Chip Design for Protein Factor Detection

To perform experiments, the operator would load genetically modified yeast cells in the sample reservoir, which would be pumped through the detection region, and classified based on cell morphology as S phase, or not-S phase, and sorted accordingly. After 2~3 minutes of operation the cytometer would have sorted about 200 cells and stored them in the exit chambers. Then the forward pumping would be stopped, the sample channel sealed, the reverse waste channel opened, and the cells stored in the exit chambers would be pumped back

through the detection region again to be scanned for fluorescence. The operator could check both the S phase cells and the not-S phase cells for fluorescence independently. Once all the stored cells were re-scanned, forward pumping could start again to test more cells.

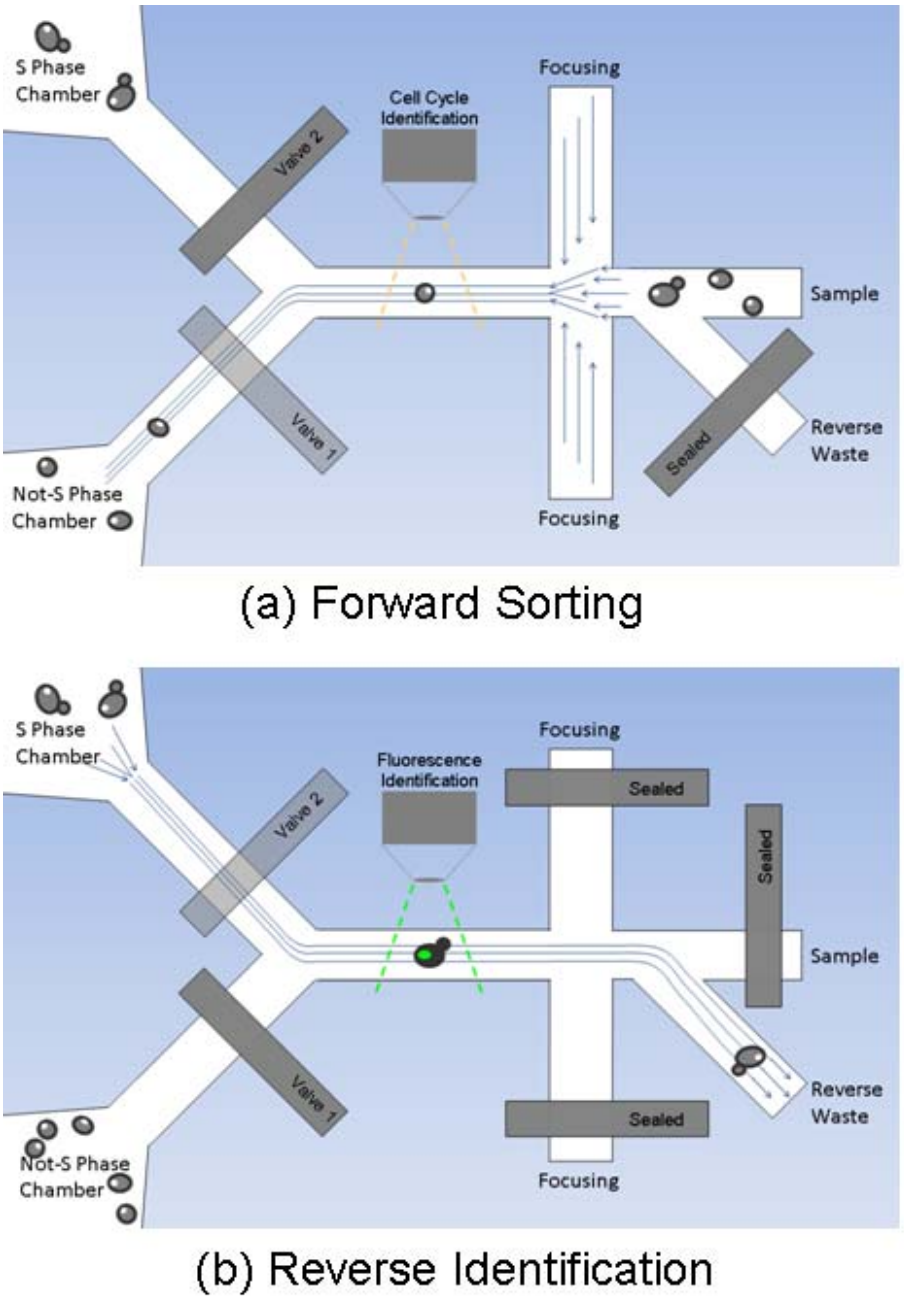

Figure 50 Operating Schematic of Proposed Experiment

The major challenge to performing this experiment would be from the biological side involving the identification of protein factors and modification of yeast cell strain. The biggest concern regarding the mechanical setup would be how to retrieve all the cells stored in the exit chambers. Since the chambers had much larger cross-sectional area compared to the fluidic channels, the fluid velocity inside the chamber would be very slow, and may not generate enough drag force on the cells to propel them. Decreasing the chamber width would increase the chamber velocity, but would also decrease the number of cells that can be stored in it. Increasing the chamber length would increase the exit resistance, which could affect the focusing performance. This trade-off must be carefully considered.

An alternative operating sequence would be to reverse pump a cell immediately after the cell cycle identification for fluorescence identification. This would eliminate the need to store cells in a chamber. However, the cell cycle identification would require the use of bright-field microscopy, while fluorescence detection used a special filter and different lighting environment, thus the microscope itself must be completely automated for this operating sequence, whereas for the previous one, the operator could manually change the settings when the detection mode is switched every 2~3 minutes.

Beside the above mentioned challenge, no other immediate problems associated with this cell sorter could be found. Areas of improvement in the future should focus on increasing the throughput of the system. Currently the cell sorter could only achieve a throughput of ~1.5 cells/second, this could be dramatically increased if better camera technology was possible. With the continued development of camera technologies and the availability of faster computing devices, imaging detection throughput should be able to compete with optical detection in the near future.

Ending Remark

Sixteen months ago, I – a new graduate of a five year Mechatronics Engineering undergraduate program at UW – set off with the goal of bringing the best, most famous microvalve system to our lab. A couple months into my project, the idea of making a microfluidic system with intelligence came into my mind, and thus the beginning of the flow cytometry project. A microfluidic chip may not be the typical artificial intelligence robot we are accustomed to in popular culture, nonetheless, it is a machine with human-like traits: it observes, it thinks, and it takes responsible actions based on its decisions. This study is intended to create a tool that is capable of performing biological analyses like a lab technician, yet along the road of creating something human like, we can find deeper meanings of our own human nature.

References

Andersson, H. and A. van den Berg (2003). "Microfluidic devices for cellomics: a review." Sensors and Actuators B-Chemical **92**(3): 315-325.

Armani, D., C. Liu, et al. (1999). "Re-configurable fluid circuits by PDMS elastomer micromachining." Mems '99: Twelfth Ieee International Conference on Micro Electro Mechanical Systems, Technical Digest: 222-227 658.

Ateya, D. A., J. S. Erickson, et al. (2008). "The good, the bad, and the tiny: a review of microflow cytometry." Analytical and Bioanalytical Chemistry **391**(5): 1485-1498.

Baret, J. C., O. J. Miller, et al. (2009). "Fluorescence-activated droplet sorting (FADS): efficient microfluidic cell sorting based on enzymatic activity." Lab on a Chip **9**(13): 1850-1858.

Bayraktar, B., P. P. Banada, et al. (2006). "Feature extraction from light-scatter patterns of Listeria colonies for identification and classification." Journal of Biomedical Optics **11**(3).

Bazzani, A., A. Bevilacqua, et al. (2001). "An SVM classifier to separate false signals from microcalcifications in digital mammograms." Physics in Medicine and Biology **46**(6): 1651-1663.

BD. (2009). "BD FACSCalibur Flow Cytometry System Technical Specifications." Retrieved July 9, 2010, from http://www.bdbiosciences.com/documents/FACSCalibur_FlowCytometry_TechSpec.pdf.

Bittner, C., G. Wehnert, et al. (1998). "In situ microscopy for on-line determination of biomass." Biotechnology and Bioengineering **60**(1): 24-35.

Chen, K. C., L. Calzone, et al. (2004). "Integrative analysis of cell cycle control in budding yeast." Molecular Biology of the Cell **15**(8): 3841-3862.

Choi, S. and J. K. Park (2005). "Microfluidic system for dielectrophoretic separation based on a trapezoidal electrode array." Lab on a Chip **5**(10): 1161-1167.

Chou, H. P., Unger, M.A., Quake, S.R. (2001). "A microfabricated rotary pump." Biomedical Microdevices. **3**(323): 30.

Devijver, P. A. and J. Kittler (1982). Pattern recognition : a statistical approach. Englewood Cliffs, N.J., Prentice/Hall International.

Dittrich, P. S., K. Tachikawa, et al. (2006). "Micro total analysis systems. Latest advancements and trends." Analytical Chemistry **78**(12): 3887-3907.

Fu, A. Y., H.-P. Chou, et al. (2002). "An Integrated Microfabricated Cell Sorter." Analytical Chemistry **7**(11): 2451-2457.

Fu, A. Y., C. Spence, et al. (1999). "A microfabricated fluorescence-activated cell sorter." Nature Biotechnology **17**(11): 1109-1111.

Fu, L. M., R. J. Yang, et al. (2004). "Electrokinetically driven micro flow cytometers with integrated fiber optics for on-line cell/particle detection." Analytica Chimica Acta **507**(1): 163-169.

Godin, J., V. Lien, et al. (2006). Integrated fluidic photonics for multi-parameter in-plane detection in microfluidic flow cytometry. 2006 IEEE LEOS Annual Meeting Conference Proceedings, Vols 1 and 2. New York, Ieee**:** 605-606.

Gokturk, S. B., C. Tomasi, et al. (2001). "A statistical 3-D pattern processing method for computer-aided detection of polyps in CT colonography." Ieee Transactions on Medical Imaging **20**(12): 1251-1260.

Hartwell, L. H. (1974). "Saccharomyces-Cerevisiae Cell-Cycle." Bacteriological Reviews **38**(2): 164-198.

Herskowitz, I. (1988). "Life-Cycle of the Budding Yeast Saccharomyces-Cerevisiae." Microbiological Reviews **52**(4): 536-553.

Hong, J. W., V. Studer, et al. (2004). "A nanoliter-scale nucleic acid processor with parallel architecture." Nature Biotechnology **22**(4): 435-439.

Huh, D., W. Gu, et al. (2005). "Microfluidics for flow cytometric analysis of cells and particles." Physiological Measurement **26**(3): R73-R98.

Ingalls, B. P., B. P. Duncker, et al. (2007). "Systems Level Modeling of the Cell Cycle Using Budding Yeast." Cancer Information **3**: 357-370.

Johann, R. and P. Renaud (2004). "A simple mechanism for reliable particle sorting in a microdevice with combined electroosmotic and pressure-driven flow." Electrophoresis **25**(21-22): 3720-3729.

Kang, Y. J., X. D. Wu, et al. (2008). "On-chip fluorescence-activated particle counting and sorting system." Analytica Chimica Acta **626**(1): 97-103.

Kartalov, E. P., A. Scherer, et al. (2007). "Experimentally validated quantitative linear model for the device physics of elastomeric microfluidic valves." Journal of Applied Physics **101**(6): -.

Koschwanez, J., M. Holl, et al. (2004). "Identification of budding yeast using a fiber-optic imaging bundle." Review of Scientific Instruments **75**(5): 1363-1365.

Kovac, J. R. and J. Voldman (2007). "Intuitive, image-based cell sorting using optofluidic cell sorting." Analytical Chemistry **79**(24): 9321-9330.

Landers, J. P. (2008). Handbook of capillary and microchip electrophoresis and associated microtechniques. Boca Raton, CRC Press.

Lee, G. B., C. H. Lin, et al. (2005). "Micromachine-based multi-channel flow cytometers for cell/particle counting and sorting." Journal of Micromechanics and Microengineering **15**(3): 447-454.

Lee, P. J., N. C. Helman, et al. (2008). "A microfluidic system for dynamic yeast cell imaging." Biotechniques **44**(1): 91-95.

Lin, C. H., G. B. Lee, et al. (2004). "Vertical focusing device utilizing dielectrophoretic force and its application on microflow cytometer." Journal of Microelectromechanical Systems **13**(6): 923-932.

Lin, Y. H. and G. B. Lee (2008). "Optically induced flow cytometry for continuous microparticle counting and sorting." Biosensors & Bioelectronics **24**(4): 572-578.

Mao, X. L., S. C. S. Lin, et al. (2009). "Single-layer planar on-chip flow cytometer using microfluidic drifting based three-dimensional (3D) hydrodynamic focusing." Lab on a Chip **9**(11): 1583-1589.

Marcus, J. S., W. F. Anderson, et al. (2006). "Microfluidic single-cell mRNA isolation and analysis." Analytical Chemistry **78**(9): 3084-3089.

Melin, J. and S. R. Quake (2007). "Microfluidic large-scale integration: The evolution of design rules for biological automation." Annual Review of Biophysics and Biomolecular Structure **36**: 213-231.

Moon, I. and B. Javidi (2006). "Volumetric three-dimensional recognition of biological microorganisms using multivariate statistical method and digital holography." Journal of Biomedical Optics **11**(6): 7.

Niemisto, A., M. Nykter, et al. (2007). "Computational Methods for Estimation of Cell Cycle Phase Distributions of Yeast Cells." EURASIP Journal on Bioinformatics and Systems Biology.

Ohnuki, S., S. Nogami, et al. (2009). "A microfluidic device to acquire high-magnification microphotographs of yeast cells." Cell Div **4**: 5.

Ohtani, M., A. Saka, et al. (2004). "Development of Image Processing Program for Yeast Cell Morphology." Journal of Bioinformatics and Computational Biology **1**(4): 695-709.

Otsu, N. (1979). "Threshold Selection Method from Gray-Level Histograms." Ieee Transactions on Systems Man and Cybernetics **9**(1): 62-66.

Pandolfi, A. and M. Ortiz (2008). "Numerical analysis of elastomeric fluidic microvalves." Sensor Letters **6**(1): 43-48.

Rieseberg, M., C. Kasper, et al. (2001). "Flow cytometry in biotechnology." Applied Microbiology and Biotechnology **56**(3-4): 350-360.

Shapiro, H. M. (1995). Practical flow cytometry. New York, Wiley-Liss.

Sidorova, J. M. and L. L. Breeden (2003). "Precocious G1/S transitions and genomic instability: the origin connection." Mutation Research-Fundamental and Molecular Mechanisms of Mutagenesis **532**(1-2): 5-19.

Simonnet, C. and A. Groisman (2006). "High-throughput and high-resolution flow cytometry in molded microfluidic devices." Analytical Chemistry **78**(16): 5653-5663.

Srivastava, S., J. J. Rodriguez, et al. (2008). "Computer-aided identification of ovarian cancer in confocal microendoscope images." Journal of Biomedical Optics **13**(2).

Studer, V., G. Hang, et al. (2004). "Scaling properties of a low-actuation pressure microfluidic valve." Journal of Applied Physics **95**(1): 393-398.

Tai, C. H., S. K. Hsiung, et al. (2007). "Automatic microfluidic platform for cell separation and nucleus collection." Biomedical Microdevices **9**(4): 533-543.

Taylor, J. K., C. L. Ren, et al. (2008). "Numerical and experimental evaluation of microfluidic sorting devices." Biotechnology Progress **24**(4): 981-991.

Theodoridis, S. and K. Koutroumbas (1999). Pattern recognition. San Diego, CA ; London, Academic Press.

Thorsen, T., S. J. Maerkl, et al. (2002). "Microfluidic large-scale integration." Science **298**(5593): 580-584.

Unger, M. A., H. P. Chou, et al. (2000). "Monolithic microfabricated valves and pumps by multilayer soft lithography." Science **288**(5463): 113-116.

Voldman, J., M. L. Gray, et al. (2002). "A microfabrication-based dynamic array cytometer." Analytical Chemistry **74**(16): 3984-3990.

Wang, Z., J. El-Ali, et al. (2004). "Measurements of scattered light on a microchip flow cytometer with integrated polymer based optical elements." Lab on a Chip **4**(4): 372-377.

Wolff, A., I. R. Perch-Nielsen, et al. (2003). "Integrating advanced functionality in a microfabricated high-throughput fluorescent-activated cell sorter." Lab on a Chip **3**(1): 22-27.

Yamaguchi, N., M. Sasada, et al. (2003). "Rapid detection of respiring Escherichia coli O157 : H7 in apple juice, milk, and ground beef by flow cytometry." Cytometry Part A **54A**(1): 27-35.

Appendix A. Micro-Fabrication Protocols

A1 Photolithography fabrication of the flow layer mold with semi-circular channels

This procedure will produce ~20μm thick rounded features that are hydrophobic, and ready for PDMS casting.

Pre-lab1 Take the AZ50XT photoresist from the refrigerator at least 2 hours before fabrication.
(if the dispensing tube is empty, pour from the bottle into the tube, and keep the original bottle in the refrigerator at all times)

Pre-lab2 turn on the two hotplates to 115C and 85C, let them reach steady temperature

Dehydration Place silicon wafer on the 115C hotplate for ~20 minutes, then let it cool to room temperature

HDMS coating Place wafer in spin coater, add few drops of HDMS to cover the surface, then spin at 1000rpm for 30sec.

Spin coating1 Enter the following recipe:

1. 0 - 500 @ 100rpm/s for 30~60 sec (depending on your skill)
2. 500 - 3000 @ 300rpm/s for 52 sec (20μm thickness)

Spin coating2 Place wafer in spinner, start spinning, dispense AZ50XT during step 1.

1. Use 14G tip and set the dispenser pressure to 15psi
2. Dispense until the photoresist covers half of the wafer. Avoid wasting photoresist

Soft Bake1 After spinning is completed, move wafer onto 85C hotplate and keep for 2 minutes

Soft Bake2 Then move to 115C hotplate for 4 minutes

Soft Bake3 Remove from hotplate and wait for >1 hour, keep wafer covered at all time

The above steps take ~40 minutes to complete. If time is limited, the operator can stop at this point, leave the wafer overnight, and resume fabrication the next day.

Exposure1 Turn on UV exposure system, set dosage to 2500 mJ/cm^2 (20μm thickness)

Exposure2 Change the wafer holder cover to a complete blank transparency (optional, this allows complete removal of non-feature photoresist)

Exposure3 Place mask on top of wafer, into the wafer holder, apply vacuum to secure in place. Start exposure. Apply complete dosage in one burst.

Development Submerge wafer in 1:3 AZ400K developer (1 developer : 3 UP water) until all undesired photoresist dissolve away, usually 4 minutes or more, depending on the condition of developer. Wash with water afterward.
Do not wash wafer with any solvent (acetone, alcohol) at any time

Silanization Place wafer in a vacuum dessicator along with a few drops of Tridecafluoro-1,1,2,2-tetrahudroctyl Triethoxy Silane on the side (the chemical can be pre-allocated into small plastic tube and sealed with N_2). Turn on the vacuum pump for ~ 2 minutes, then leave for >30 minutes. (ideally 2~3 hours)

Rounding slowly heat the wafer to 125C (steps of 50C, 80C, 100C, 125C at 10 min intervals on the small hotplate) and bake for 30 minutes. Then cool down in two steps (80C and off)

Fabrication Completed

A2: Photolithography fabrication of the control layer mold with 40um channel height

This procedure will produce ~40µm thick SU-8 features with an SU-8 sacrificial layer

Pre-lab1 Pour SU-8 2005 and SU-8 2025 from the original bottle into dispensing tube the **day before** fabrication to allow bubbles to disperse. (wipe bottle opening with acetone to prevent photoresist sticking to the cap)

Pre-lab2 turn on the two hotplates to 95C and 65C, turn on small hotplate to 200C, let them reach steady temperature

Dehydration Place silicon wafer on the 200C hotplate for ~10 minutes, then let it cool to room temperature

Pre-lab3 after dehydration, turn small hotplate down to 50C

SU-8 2005 Adhesion Layer (~ 5µm thick)

Spinning Enter the spin recipe: 0 – 2000 rpm @ 500 r/s for 35 sec
Dispense SU-8 2005 statically, using the recommended tip & pressure
Start spin coater

Soft bake 65C for 1 min
95C for 2 min
65C for 30 sec
Cool down to room temperature

Exposure place wafer **on top** of the mask holder, **do not cover** wafer with mask, and apply dosage 250 mJ/cm^2

Post bake 65C for 1 min
95C for 3 min
65C for 30 sec
Cool down to room temperature

Adhesion layer complete, operator can stop here and resume next day if time is limited

SU-8 2025 Feature Layer (~ 40µm thick)

Spinning Enter recipe:
1. 0-500 @ 100r/s for 50 sec
2. 500-1800 @300r/s for 35 sec

Start spin coater
Dispense SU-8 2025 dynamically during step 1, use recommended tip & pressure

Soft bake	65C for 3 min 95C for 6 min 65C for 30 sec Cool down to room temperature
Exposure	Place wafer **into** the mask holder, with mask covering the wafer. Apply dosage 630 mJ/cm^2
Post bake	65C for 1 min 95C for 6 min 65C for 30 sec 50C for 30 sec Place wafer on cold glass surface, and **leave it for 2~3 hour**s allowing it to completely reach equilibrium at room temperature
Development	Submerge wafer in SU-8 developer (PGMEA, poison solvent, take adequate safety measure) for 5 minutes. Bring out of developer and wash with fresh SU-8 developer and water alternately until surface is free of impurities.

Fabrication complete. SU-8 is hydrophobic on its own, but silanization is recommended. Follow the same procedure as A1.

A3: Multi-layer soft lithography fabrication of PDMS microchip

This procedure is for making 2-layer PDMS chip. Requires pre-fabricated control layer mold and a fluidic layer mold.

Mix 10g of 20:1 PDMS and 50g of 5:1 PDMS separately and degas them.

Place the bottom layer mold (control layer) on the spin chuck, and spincoat the 20:1 PDMS at a speed of 1600rpm for 50 sec.

Let the PDMS sit on a flat surface for 30 minutes to make the PDMS surface smooth.

Pour three quarter of the 5:1 PDMS on the top layer mold (fluidic layer), and place it on 80C hotplate (or 80C oven) for **10~12 minutes** to let the PDMS cure slightly until it just harden. Remove from hotplate and let it cool.

Peel off the fluidic layer PDMS, cut it into desired shape, punch access holes to the fluidic layer channels using the 14G tip. Once the fluidic layer is ready, place the control layer on 80C hotplate (or oven) for **16~18 minutes**, remove from hotplate and bond the fluidic layer to it immediately. DO NOT over bake. The PDMS will stick to each other without plasma treatment.

Pour the remaining 5:1 PDMS on the control layer mold, around the newly bonded fluidic layer, and bake on 80C hotplate for another 2~3 hrs to complete the curing reaction. By pouring additional PDMS on the control layer it allows easy peel off of the chip, otherwise the membrane may be too thin to grab onto.

After the PDMS is peeled off, cut it into the desired chip shape, and punch access holes to the control layer using 18G (light green) tips. The PDMS may tear during hole-punching, and may cause air leakage. If leakages occur, plug hole with 22G (light blue) tip, and add a drop of PDMS on the hole to cover the leak.

Appendix B. Controller Design Documents

B1: PCB layout and bill of material

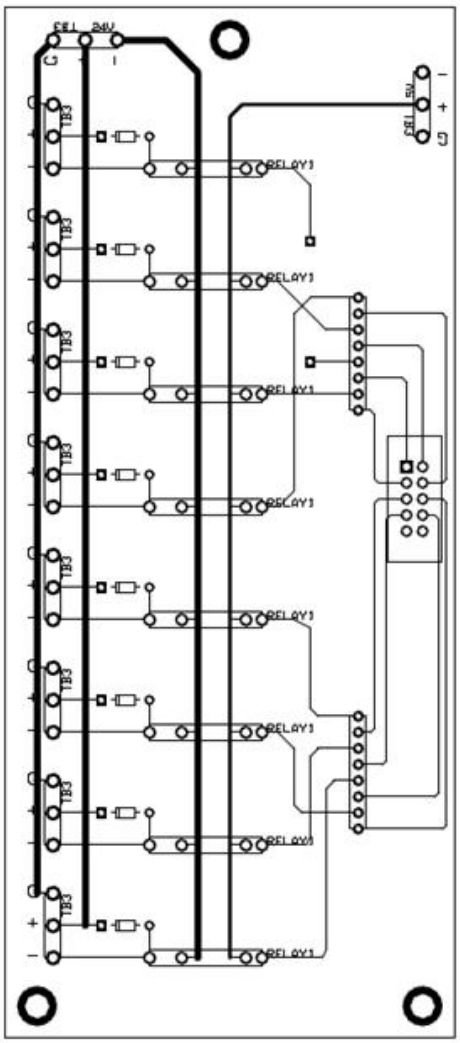

	Bill of Material		
No	**Desription**	**Digikey #**	**Quantity**
1	male/Female threaded standoff 0.25 length 4-40 aluminum	8714K-ND	3
2	Terminal block 5mm 3pos	ED1624-ND	10
3	Diode Schottky 30V 200mA	568-1617-1-ND	8
4	Relay Optomos 0.35A 4-sip	CLA211-ND	8
5	Resistor pack 4res 330ohm 8pin	770-83-R330P-ND	2
6	shrouded header 10 pos straight	MHC10E-ND	1
7	piece of wire		1

B2: RTOS pseudo code

User defined interrupts: time_interrupt()

User defined functions: update_pump()
update_valve()

User defined structure: pump_block
{ is_ON, direction, speed}

Global Variables:

arrays:
base_pumping_sequence[4]
port_sequence_value[32]
old_sequence_value[32]
new_sequence_value[32]

integer:
sequence_index
base_period
timer_count

```
void main()
{
        initialize 8 pump_block objects;
        initialize a 32 element array as valve_block;
        assign values to global arrays:
                base_pumping_sequence = [3 6 4 5]
                sequence_values = [0]
        initialize hardware, start timer

        while(true)
                if there is serial data coming in (poll for serial input)
                        check if data is for pump:
                                decode data, update the corresponding pump_block
                                update_pumps();
                        if data is for a valve:
                                decode data, update the corresponding valve_block
                                update_valves();
                        if data is for changing timer period
                                base_period = serial data;

}

void timer_init()
```

```
{ initialize timer, provided by supplier}

void timer_interrupt()
{
        timer_count ++;
        if  timer_count >= base_period  // timer expired
                reset timer_count

                check if sequence_index > 32, if so, reset sequence_index

                // write to hardware IO pins
                port = port_sequence_value[sequence_index]

                sequence_index++;

}

void uart_init()
{ initialize serial communication, provided by supplier}

void update_pump(id, old_pump_block, new_pump_block)
{

        calculate the corresponding 32-element sequence for the old pump_block, based on
        speed and direction
        calculate the corresponding 32-element sequence for the new pump_block, based on
        speed and direction
        subtract the old sequence from port_sequence_value, add the new sequence to
        port_sequence_value
}

void update_valve(id, old_valve_element, new_valve_element)
{
        find the modifier of the valve based on id.
        Subtract old_valve_element*modifier from port_sequence_value
        Add new_valve_element*modifier to port_sequence_value
}
```

Appendix C. Experimental Protocols

C1: Recommended sizes for reservoir, connectors, and tubing

All holes are punched with EFD dispensing metal tips as punchers. The connectors are also EFD metal tips with the metal tube removed from the plastic base. All tubing purchased from Cole & Parmer company.

Control channel reservoir:

- punch with 18GA x0.25" tip
- connect using 20GA 90deg tip
- Connect to solenoid valve using silicone tubing 1.14mm ID

Fluidic channel reservoir:

- punch with 14GAx0.25" tip
- reservoir usually open to air
- For bubble removal, using 18GA 90deg tip, connect with TYGON .02x.06" tubing